Forward Model and Jacobians for Tropospheric Emission Spectrometer Retrievals

Shepard A. Clough, Mark W. Shephard, John Worden, Patrick D. Brown, Helen M. Worden, Mingzhao Luo, Clive D. Rodgers, Curtis P. Rinsland, Aaron Goldman, Linda Brown, Susan S. Kulawik, Annmarie Eldering, Michael Lampel, Greg Osterman, Reinhard Beer, Kevin Bowman, Karen E. Cady-Pereira, and Eli J. Mlawer

***Abstract*—The Tropospheric Emission Spectrometer (TES) is a high-resolution spaceborne sensor that is capable of observing tropospheric species. In order to exploit fully TES's potential for tropospheric constituent retrievals, an accurate and fast operational forward model was developed for TES. The forward model is an important component of the TES retrieval model, the Earth Limb and Nadir Operational Retrieval (ELANOR), as it governs the accuracy and speed of the calculations for the retrievals. In order to achieve the necessary accuracy and computational efficiency, TES adopted the strategy of utilizing precalculated absorption coefficients generated by the line-by-line calculations provided by line-by-line radiation transfer modeling. The decision to perform the radiative transfer with the highest monochromatic accuracy attainable, rather than with an accelerated scheme that has the potential to add algorithmic forward model error, has proven to be very successful for TES retrievals. A detailed description of the TES forward model and Jacobians is described. A preliminary TES observation is provided as an example to demonstrate that the TES forward model calculations represent TES observations. Also presented is a validation example, which is part of the extensive forward model validation effort.**

***Index Terms*—Earth Limb and Nadir Operational Retrieval (ELANOR), forward model, Jacobians, line-by-line radiation transfer modeling (LBLRTM), radiative transfer (RT), TES, Tropospheric Emission Spectrometer (TES).**

I. Introduction

THE Tropospheric Emission Spectrometer (TES), launched on July 15, 2004 on the Earth Observing System (EOS) Aura satellite, was developed to provide continuous global surveys of the chemical state of the troposphere. TES is a spaceborne high-resolution Fourier transform spectrometer that covers the infrared spectral range 650–3050 cm^{-1} with both limb and nadir viewing capabilities and a spectral resolution of 0.025 and 0.06 cm^{-1}, respectively [1]. Another characteristic of the TES instrument is that it utilizes interchangeable filters for different spectral subregions (filters shown in Table I).

TABLE I
SPECTRAL GRIDS FOR TES FILTERS

Filter ID	Lower Point (cm^{-1})	Upper Point (cm^{-1})	Reference Grid (cm^{-1})	Operational Spectral Grid (cm^{-1})
1A1	1900	2250	0.0004	0.0008
1A2	2200	2450	0.0004	0.0008
1A3	2425	2650	0.0004	0.0008
1A4	2600	2850	0.0004	0.0008
1A5	2800	3050	0.0004	0.0008
1B1	820	1050	0.0002	0.0004
1B2	950	1150	0.0002	0.0004
2A1	1100	1325	0.0002	0.0004
2A2	1300	1550	0.0002	0.0004
2A3	1500	1750	0.0002	0.0004
2A4	1700	1950	0.0002	0.0004
2B1	650	900	0.0001	0.0002

The high-quality TES observations require that the TES operational retrieval model, Earth Limb and Nadir Operational Retrieval (ELANOR), be both accurate and computationally efficient. The TES operational retrieval model originated with a pilot code developed at Atmospheric and Environmental Research, Inc. (AER). The forward model component is based on the line-by-line radiation transfer model (LBLRTM) [2], itself based on the FASCODE line-by-line model [3]. This algorithm was then updated by the Jet Propulsion Laboratory (JPL) to the TES Working Prototype Retrieval algorithm (TWPR) for operational prototyping and testing. These prototyping efforts proved to be valuable in testing the speed and accuracy of algorithms forwarded by the members of the TES Science Team. The present ELANOR operational algorithm was developed based on the design of TWPR. An important component of ELANOR is the forward model, as it determines the accuracy and speed of the calculations.

The retrieval strategy for TES utilizes the method of minimized variance in which the variance is taken between the measured spectral radiances and those obtained from a forward model [4]–[6]. The role of the forward model is to calculate accurate spectral radiances equivalent to those measured by the spectral radiometer given a forward model state vector including inputs characterizing the radiating atmosphere and surface. The forward model also includes the characterization of the instrument to enable direct comparison of the measured and calculated radiances. A critical requirement for the forward model is that it be as accurate as possible and yet be capable of performing the calculations with acceptable computational cost. For aspects

Manuscript received May 23, 2005; revised October 7, 2005. This work was supported by funding for the National Aeronautics and Space Administration (NASA) TES Science Team under a contract with the Jet Propulsion Laboratory, lifornia Institute of Technology.

S. A. Clough, M. W. Shephard, K. E. Cady-Pereira, and E. J. Mlawer are with Atmospheric and Environmental Research, Inc. (AER), Lexington, MA 02421-3126 SA (e-mail: sclough@ aer.com; mshephar@aer.com).

P. D. Brown was with Atmospheric and Environmental Research, Inc. (AER), Lexington, MA 02421-3126 SA. He is now with Hartford Financial Services Group, Hartford, CT 06115 USA.

J. Worden, H. M. Worden, A. Eldering, M. Luo, L. Brown, S. Sund-Kulawik, G. Osterman, R. Beer, and K. Bowman are with the Jet Propulsion Laboratory, California Institute of Technology, Pasadena, CA 91109 USA.

C. D. Rodgers is with Oxford University, Clarendon Laboratory, Oxford, OX1 3PU, U.K.

C. P. Rinsland is with NASA Langley Research Center, Hampton, VA 23681-3142 USA.

A. Goldman is with the University of Denver, Denver, CO 80208 USA.

M. Lampel is with Raytheon Technical Services Co., LLC, Pasadena, CA 91101 USA.

Digital Object Identifier 10.1109/TGRS.2005.860986

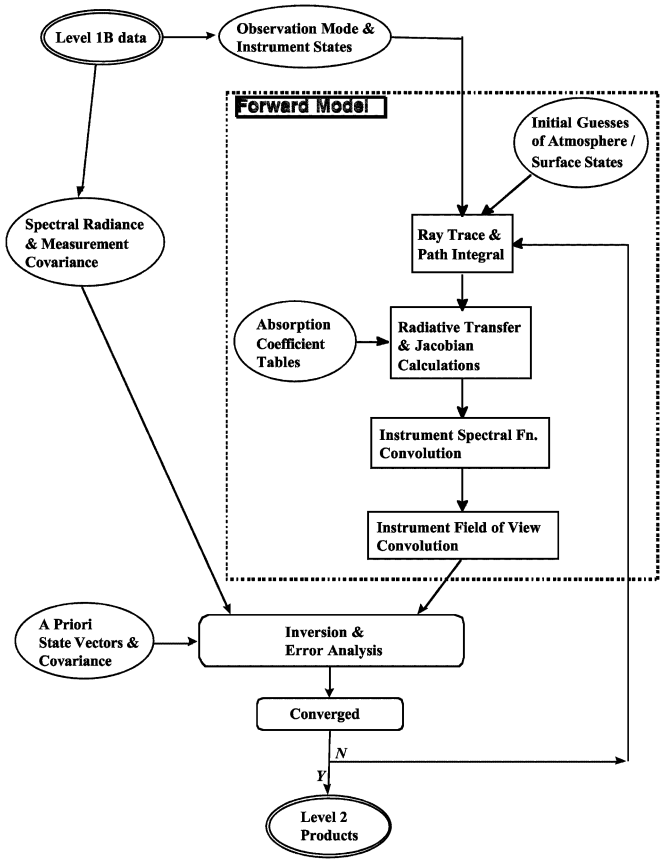

Fig. 1. Flow diagram of the overall TES level 2 retrieval algorithm.

of the retrieval problem, errors in the forward model including errors in the line parameters, systematic in nature, may be a significant contributor to the retrieval error. The context for the forward model is provided in Fig. 1. The overall retrieval strategy is indicated together with the role of the forward model in that context. The differences between the measured and calculated spectral radiances, the variance of which is to be minimized by adjustment of the state vector, are contained in the box labeled "Inversion & Error Analysis."

The pressure level and spectral grids used in the TES forward model calculations are specified and a detailed description of the important components of the forward model is presented. The modules of particular importance for the forward model are those required to perform the ray tracing and layer path integrals; the radiative transfer (RT) including the optical depth calculations, the Jacobians of the spectral radiances with respect to specified parameters; the convolution of the calculated monochromatic spectrum with the spectral instrumental function; and in the case of the limb, the convolution of the radiance field characterized by rays associated with multiple tangent pressures with the instrument field of view. A state vector is required for the forward model that includes the temperature profile, profiles for relevant molecular species, cloud and aerosol characteristics, and the parameters necessary to describe the radiative properties of the surface. In Fig. 1, these state vector elements are indicated by the oval "Initial Guesses of Atmospheric/Surface States."

The following sections describe the key elements of the forward model and Jacobian modules. The content for these sections follows closely the detailed description in the TES ATBD [7] with appropriate modifications and summaries.

II. Forward Model

A. Pressure Level and Spectral Grids

Before describing in detail the TES forward model calculations we must specify the TES forward model pressure levels and spectral grids on which the calculations will be performed. The natural vertical grid for the forward model is based on pressure levels, as this variable has a more basic connection to atmospheric state and is one for which the Jacobians have a particularly simple form. A common pressure grid has been chosen for the limb and nadir measurements. The spacing of the vertical levels is determined by two considerations: 1) accuracy of the forward model radiative transfer calculation and 2) the angular distribution of the limb radiances arriving at the satellite for the finite field of view convolution. The basic vertical coordinate is chosen as $\log(P)$ and the spacing has been made compatible with that established for Upper Atmospheric Research Satellite (UARS).

The forward model state vector is defined on the *full grid* by

$$\log_{10}(P_i) = \frac{5-i}{6m} \tag{1}$$

which provides a superset of the UARS grid, where P_i is the pressure in hPascals of level index i and the "superset factor" m is an integer. The UARS grid corresponds to $m = 1$, with a spacing of six levels per decade of pressure. The value of m is determined by the accuracy requirements of the numerical method.

The full state vector defines an 86-layer atmosphere for the absorption coefficient table pressure and temperature grids. This 86-layer atmosphere has 87 pressure levels between 1211.53 and 0.1 hPa. The pressure levels (in hPa) are defined up to 1 hPa ($m = 4$) as

$$P_k = 1000 \times 10^{-(k-2)/24}, \qquad k = 0, \ldots, 74 \tag{2}$$

and above 1 hPa ($m = 2$) as

$$P_k = 1000 \times 10^{-(k-38)/12}, \qquad k = 75, \ldots, 86. \tag{3}$$

In the troposphere, the geometric layer thickness for the U.S. standard atmosphere varies from 0.83 km (surface) to 0.6 km (tropopause). Between 100 and 1 hPa, the layer thickness is 0.6–0.8 km; while above 1 hPa, it is 1.5 km.

The pressure at the Earth's surface provides the lower boundary for the forward model and is defined for every TES observation. The layer with the surface as its lower boundary is thinner than (or equal to) a TES standard forward model layer. The sea surface pressure is obtained from available meteorological data [e.g., Global Modeling and Assimilation Office (GMAO)]. The Earth surface pressure is calculated from the sea surface pressure using the hydrostatic equation at the surface geodetic elevation. The top pressure boundary for the surface layer is a TES fixed pressure level.

The spectral grid for the monochromatic radiative transfer calculations for the spectral domain associated with a specific

TABLE II
NOMINAL GRID SPACING VALUES OF OTHER SPECTRAL PARAMETERS

Parameter	Spectral Grid Spacing (cm^{-1})
Heavy molecules (e.g., HNO_3, CFC's)	0.0025
H_2O, CO_2, N_2, and O_2 continua	0.1
Clouds and aerosols	1.0
Surface emissivity	10.0
Surface albedo/reflectivity	10.0
Surface bi-directional reflectivity distribution function	10.0

TES filter is determined by the mean Doppler width at the top of the atmosphere. Studies of the dependence of errors in RT on spectral sampling indicate that for pressure broadened lines, a sampling grid of four points per Lorentz halfwidth is required [8] for acceptable monochromatic accuracy. Extension of this analysis to the Doppler and Voigt line shapes leads to effectively the same conclusion. The spectral sampling based on this criterion, in addition to being appropriate for the stratosphere, provides proper spectral sampling of the narrow water lines in the atmospheric window regions and of the line coupling effects of the carbon dioxide Q branches in the pressure-broadening regime. The spectral grid is based on the Doppler width, but is fixed for a given filter.

The archived absorption coefficient files, described in detail in Section III, are computed for a spectral grid of four points per halfwidth at the top of the atmosphere. To reduce computational cost and data storage for the operational retrievals, an operational grid that is half the resolution of the fine grid is utilized. The operational grid absorption coefficient tables are obtained by convolving a three-point triangular filter with the fine-grid tables. It was determined that the instrument convolved radiances computed using this operational grid are accurate to within 0.001% as compared with the radiances computed using the fine spectral grid. Table I describes the operational spectral grid for each filter. The RT parameters specified on other spectral grids (e.g., spectral emissivity) are interpolated by a four-point Lagrangian to the operational spectral grid; refer to Table II.

B. Ray Tracing and Path Integrals

The first step in the TES forward model calculations is to obtain effective layer pressures and temperatures and layer column amounts by performing the required ray tracing and path integral calculations over the forward model pressure grid. The basic principles of the line of sight calculation are described here; for full details refer to the TES Level 2 Algorithm Theoretical Basic Document (ATBD) [7]. The nonsphericity of the Earth is accommodated by using a coordinate system with origin at the Earth's center of curvature at the latitude corresponding to the intersection of the nadir ray with the Earth surface for the nadir case or the latitude of the tangent point for the limb case. In the plane of the ray (refraction horizontally is ignored) the atmosphere is described in terms of functions of radius r and angle ψ of the line from the center to the ray element (see Fig. 2). Quantities in a radially symmetric atmosphere are assumed to be independent of ψ.

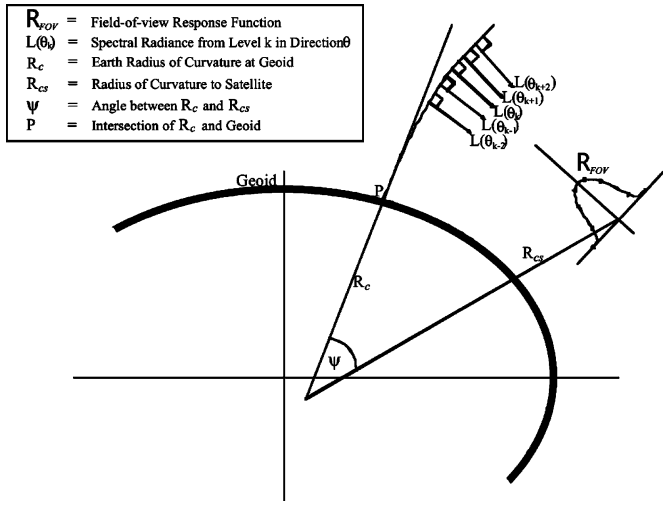

Fig. 2. Diagram for TES limb geometry and FOV convolution in limb mode.

For integrating the hydrostatic equation, a full latitude/altitude model is used for the variation of the acceleration of gravity. The air density is calculated from an equation of state that includes the effect of water, and is not simplified to the perfect gas law.

For the nadir case, the ray tracing is evaluated from simple trigonometry, ignoring refraction. Evaluations of volume mixing ratio q and temperature T are carried out analytically over full pressure P grid layers, assuming that $ln(q)$ and T are linear in $ln(P)$.

For the limb case, the approach used is based on that of Kneizys *et al.* [9]. The coordinate $x = r\cos\theta$ is used along the ray to avoid the singularity at the tangent point, where r is the radius from a center and θ is the zenith angle. The zenith angle of the ray is obtained from Snell's law for spherical symmetry, $r\, n(r)\sin\theta(r) =$ constant, and the distance element ds along the ray is related by $\mathrm{dr} = \sin\theta ds$ This provides the following relation:

$$ds = \frac{dx}{\left[1 + \left(\frac{r}{n}\right)\left(\frac{\partial n}{\partial r}\right)\sin^2\theta(r)\right]} \tag{4}$$

which is used to integrate the path integrals with respect to x, an explicit function of r, rather than s. The integrals are evaluated by dividing each full grid layer into sublayers in x, such that all quadrature intervals are smaller than a given length, and using a trapezium or higher order quadrature.

In the limb when the atmosphere is not radially symmetric, the previously outlined ray tracing technique does not apply because we can no longer assume that $n\, r \sin\theta =$ constant. In this case, we can use a more general approach and construct a set of three coupled ordinary differential equations in $r(s)$, $\theta(s)$ and $\psi(s)$ to describe the ray trajectory. These are integrated forward from an assumed tangent point to the satellite altitude. The horizontal location of the tangent point as expressed by $\psi(0)$ is then iterated so that the ray reaches the location of the satellite. Path integrals are evaluated in the same way as for the radially symmetric case, but using the same quadrature points in s as are used by differential equation integration. This refinement has been prototyped and tested by the TES Science Team.

In limb viewing mode, the angular radiation field measured by the TES detectors is represented by a number of rays that span the TES field of view (FOV) (Fig. 2). Each ray is traced through the atmosphere to the TES sensors. For those rays that do not intersect a boundary such as the Earth or a cloud, a simplification is made in the ray tracing by specifying that each ray must correspond to a tangent point of one of the TES forward model levels. Each ray's spectrum is then convolved with the TES instrument-line-shape (ILS) function to account for the TES spectral resolution. Then, the radiances from the bundle of rays are integrated over the angular response of each detector to obtain the calculated angular radiance for each of the TES detectors. The TES ray levels (or tangent levels) are specified in a ray table. The ray table specifies which levels are used for the discretized angular radiance field. There are 32 rays total in this ray table. As a test to determine the number of total rays needed, the modeled detector radiances using this set of rays was compared to the modeled detector radiances using a finer discretization of 64 rays (refer to Fig. 3). Fig. 3 shows that the difference is much less than the nominal instrument NESR; hence it is concluded that 32 rays is sufficient discretization.

An additional refinement to the TES computation of limb multiple rays is the ability to reduce the computationally expensive computation of molecular absorption coefficients and total optical depth when computing the angular radiance field. This is possible because the absorption coefficients for any given layer are approximately the same for all rays traced through the layer. If the average pressure and temperature of a layer for some ray traced through the layer is within 0.1% and 0.1 K, respectively, of that from a reference ray, then the absorption coefficients can be reused for the optical depth and Jacobian calculation, i.e.,

$$\left|\frac{1-\bar{P}_\ell^{\mathrm{ray}}}{\bar{P}_\ell^{\mathrm{ray-ref}}}\right| < 0.01$$
$$\left|\bar{T}_\ell^{\mathrm{ray}} - \bar{T}_\ell^{\mathrm{ray-ref}}\right| < 0.1\ \mathrm{K} \tag{5}$$

where ray-ref indicates a reference ray for which molecular absorption coefficients and optical depths have been computed, $\bar{P}_\ell^{\mathrm{ray}}$ and $\bar{T}_\ell^{\mathrm{ray}}$ are the average pressure and temperature, respectively, for layer ℓ and ray-index *ray*. In addition, the total layer optical depth for a given ray may be obtained from the total optical depth of a reference ray by scaling (with less than 0.1% loss in accuracy for the radiance calculation) if the above condition is met along with the additional condition that

$$\left|\frac{1-R_{\ell,\mathrm{avg}}^{\mathrm{ray}}}{R_{\ell,\mathrm{species}}^{\mathrm{ray}}}\right| < 0.001$$

where

$$R_{\ell,\mathrm{avg}}^{\mathrm{ray}} = \frac{\sum_{i=1}^{N_{\mathrm{species}}} u_{\ell,i}^{\mathrm{ray}}}{\sum_{i=1}^{N_{\mathrm{species}}} u_{\ell,i}^{\mathrm{ray-ref}}}$$
$$R_{\ell,\mathrm{species}}^{\mathrm{ray}} = \frac{u_{\ell,\mathrm{species}}^{\mathrm{ray}}}{u_{\ell,\mathrm{species}}^{\mathrm{ray-ref}}} \tag{6}$$

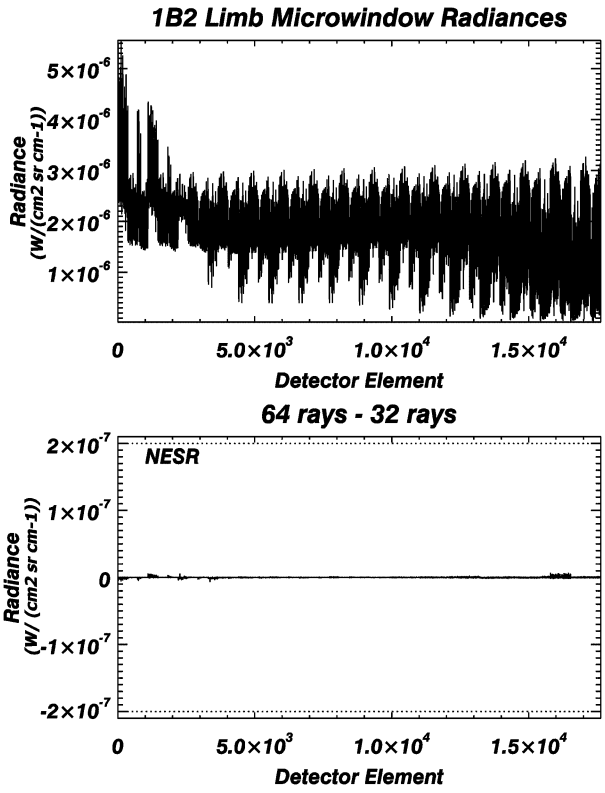

Fig. 3. Comparison of TES radiances for 1B2 filter. The top panel shows the limb angular radiances across all 16 TES detectors (1100 spectral elements per detector). The bottom panel shows that difference between radiances if 64 rays are used for the forward model calculation versus 32 rays.

and $u_{\ell,\mathrm{species}}^{\mathrm{ray}}$ is the column amount for some *species* at layer ℓ and ray index *ray*. The total optical depth for a given ray and layer ℓ can be computed by multiplying the optical depth from ray-ref and layer ℓ by the scaling factor: $R_{\ell,\mathrm{avg}}^{\mathrm{ray}}$.

C. Radiative Transfer

The spectral radiance received at the satellite is obtained by integrating the RT equation. Under clear conditions, the radiance received in a nadir-viewing mode includes four sources: upwelling atmospheric emission, reflected downwelling atmospheric emission, surface emission, and reflected solar radiation. All of these radiation sources are attenuated by the atmosphere. The monochromatic radiances are convolved with the instrument line shape (ILS) to obtain calculated radiances associated with the TES measurement. For a single ray without scattering, we have (7), shown at the bottom of the next page, where

- $L(\Omega,\nu)$ is the upwelling radiance at frequency ν into solid angle Ω;
- $\Phi(\nu,\nu')$ is the ILS, i.e., spectral response at frequency ν due to incident radiance at ν';
- $B(\nu',T)$ is the Planck function for temperature T at frequency ν';
- T_{sfc} is the surface (skin) temperature;
- $T(\Omega,z,z',\nu')$ is the atmospheric transmittance at frequency ν' in a direction Ω between altitudes z and z';
- $R_{\mathrm{BRDF}}\ (\Omega,\text{-}\Omega',\nu')$ is the surface bidirectional reflectance distribution function (BRDF) for incident (downward) solid angle Ω' and emergent (upward) solid angle Ω;

- $\epsilon(\Omega, \nu')$ is the surface emittance at frequency ν' into solid angle Ω;
- $E_s(\nu')$ is the disk-average solar radiance at frequency ν';
- Ω_s is the solar solid angle at Earth;
- z_0 is the surface altitude.

For limb viewing radiance a similar equation holds where z_0 is the tangent height, the second term is the radiance contribution from the atmosphere from the far-side space to the tangent point along the line of sight [with $R_{\mathrm{BRDF}}(\Omega, -\Omega', \nu')$ replaced by $\delta(\Omega + \Omega')$], and the last two (surface-related) terms being omitted.

The vertical integrations in (7) for the upwelling term, $L^{\uparrow}\infty$, the downwelling radiance, $L_0^{\downarrow}$, and the total transmittance $\mathcal{T}_{0,\infty}$ are calculated recursively in a loop over layers. After appropriate initialization, $L^{\uparrow}\infty$, $L_0^{\downarrow}$, and $\mathcal{T}_{0,\infty}$ are updated at each step l in the recursion as follows:

$$\mathcal{T}_{0,\infty(l+1)} = \mathcal{T}_{0,\infty(l)}\,\mathcal{T}_l \tag{8}$$

$$L^{\uparrow}_{\infty(l+1)} = L^{\uparrow}_{\infty(l)}\mathcal{T}_l + (1-\mathcal{T}_l)\,B_{\mathrm{eff}} \tag{9}$$

$$L^{\downarrow}_{0(l+1)} = L^{\downarrow}_{0(l)} + (1-\mathcal{T}_l)\,B(\bar{T}_l)\,\mathcal{T}_{0,\infty(l)} \tag{10}$$

where $\mathcal{T}_l$ is the transmittance of the layer l, $B(\bar{T}_l)$ is the Planck function at the mean temperature of layer l, and B_{eff} is the layer effective Planck function defined below [(12)].

The layer transmittance $\mathcal{T}_l$ is calculated as

$$\mathcal{T}_l = \exp(-\tau_l) \tag{11}$$

where τ_l is the layer optical depth. Since the exponential calculation is relatively expensive, it is precomputed and tabulated in a lookup table.

In order to reduce the error associated with the discretization of the problem, we apply an approximation in which the Planck function is assumed to vary linearly with optical depth through the layer, the "linear-in-tau" approximation [10]. The source term in (9) uses an effective Planck function defined as

$$B_{\mathrm{eff}}(\bar{T}_l, T_{l+1}, \tau_l) = B(\bar{T}_l) + [B(T_{l+1}) - B(\bar{T}_l)]\,F(\tau_l) \tag{12}$$

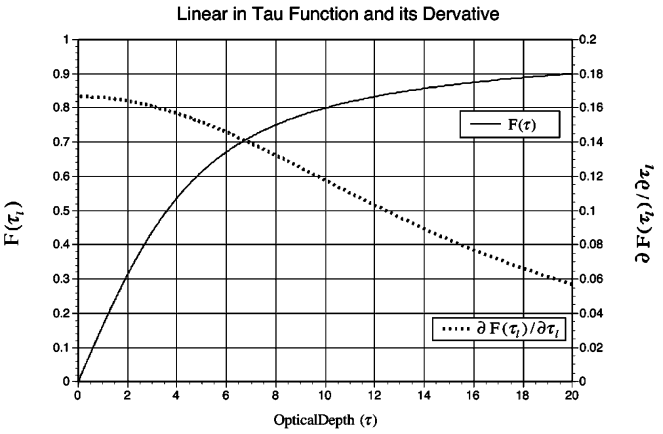

Fig. 4. Plot of the linear-in-tau function and its derivative.

where $B(T_{l+1})$ is the Planck function calculated using the layer upper level temperature, T_{l+1}. The "linear-in-tau" function

$$F(\tau_l) = 1 - 2\left[\frac{1}{\tau_l} - \frac{\mathcal{T}_l}{1-\mathcal{T}_l}\right] \tag{13}$$

and its derivative with respect to optical depth are precalculated and tabulated for computation efficiency (Fig. 4). For small optical depth, $F(\tau_l) \longrightarrow \tau/6$ as $\tau_l \longrightarrow 0$, which can be shown either graphically or by expanding $F(\tau)$ to higher order terms. This effective Planck function has the desired behavior at the two extremes [optically thin layers, $B_{\mathrm{eff}} \approx B(\bar{T}_l)$ and optically thick layers, $B_{\mathrm{eff}} \approx B(\bar{T}_{l+1})$].

The calculation of the Planck function as a function of frequency at the forward model frequency grids is computationally expensive. A piecewise continuous approximation has been utilized in this calculation. The Plank function is calculated for a coarser frequency grid and a linear interpolation is done for the intermediate spectral elements.

1) Surface Contribution: The computation of the downwelling radiance at the surface depends on the nature of the scattering due to the surface, which is characterized as either Lambertian or specular. For the Lambertian case, the surface bidirectional reflectance is independent of angle and can be expressed simply in terms of a surface albedo, which, when multiplied by the downwelling radiance computed along the

$$\begin{aligned} L(\Omega,\nu) = \int_0^{\infty} \Phi(\nu,\nu') \Bigg\{ & \int_{z_0}^{\infty} B(\nu', T(z)) \frac{\partial \mathcal{T}(\Omega, z, z_0, \nu')}{\partial z} dz \\ & \text{(Instrument)} \quad \text{(Upwelling atmospheric emission term)} \\ & + \mathcal{T}(\Omega, z_0, \infty, \nu') \int_{2\pi} R_{\mathrm{BRDF}}(\Omega, -\Omega', \nu') \int_{\infty}^{z_0} B(\nu', T(z)) \frac{\partial \mathcal{T}(-\Omega', z, z_0, \nu')}{\partial z} dz d\Omega' \\ & \text{(Downwelling, back-reflected, atmospheric emission term)} \\ & + \varepsilon(\Omega, \nu') \cdot B(\nu', T_{\mathrm{sfc}}) \cdot \mathcal{T}(\Omega, z_0, \infty, \nu') \\ & \text{(Surface emission term)} \\ & + R_{\mathrm{BRDF}}(\Omega, -\Omega_s, \nu') \cdot E_s(\nu') \cdot \Omega_s \cdot \mathcal{T}(-\Omega_s, \infty, z_0, \nu') \cdot \mathcal{T}(\Omega, z_0, \infty, \nu') \Bigg\} d\nu' \\ & \text{(Reflected sunlight term)} \end{aligned} \tag{7}$$

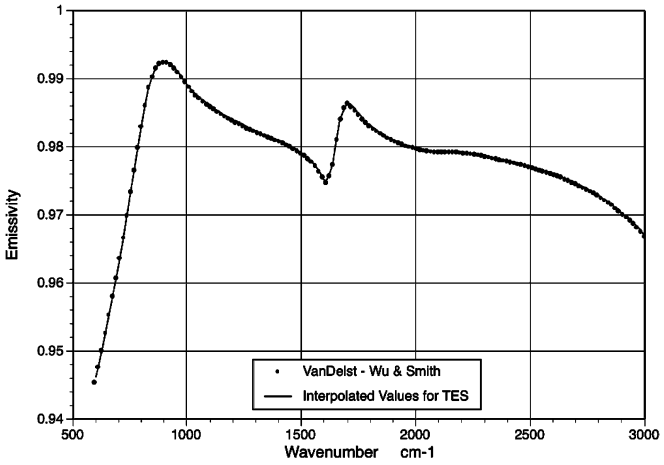

Fig. 5. Plot of the spectral sea surface emissivity. The values in the red regions have been interpolated for TES.

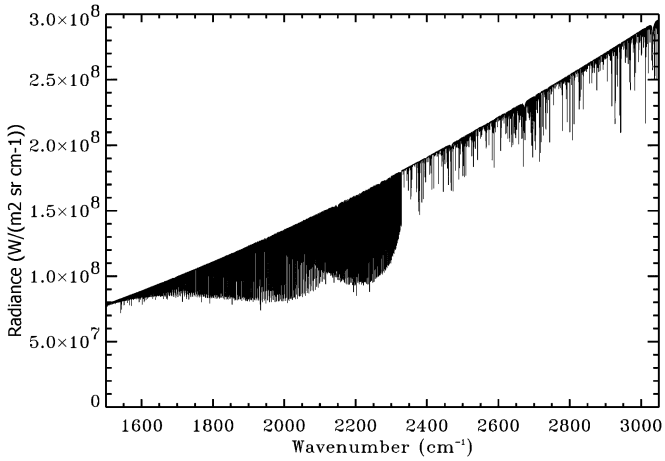

Fig. 6. Monochromatic solar spectrum over the spectral region relevant to TES.

diffusivity ray $(\text{secant} = 1.66)$ [11] provides an excellent approximation to the scattered upwelling isotropic radiance at the surface. The motivation for this approach is the low computational cost with acceptable accuracy. The layer optical depth for the diffusivity angle is obtained by multiplying the nadir layer optical depth by the secant of the diffusivity angle. Although an additional exponential is required, this approach is faster than alternative methods. In the case of specular reflection, the downwelling radiance is calculated for the same secant as the upwelling ($\text{secant} = 1$ in the nadir case) and the same layer transmittances are used for both the upwelling and downwelling radiances. This calculation is fast and has full accuracy.

The surface emissivity used in the RT calculation is determined using two methods depending on if the surface is water or land. For an ocean scene the surface is uniform over the TES FOV and the sea surface emissivity is spectrally well characterized and extensively validated [12]–[14]. The sea surface spectral emissivity being utilized by TES is that of Wu and Smith (see Fig. 5) [12], which is available as a function of wind speed and viewing angle. Over land the surface emissivity is retrieved from the TES nadir data, which has many spectral regions that contain information about the surface radiative properties ("window" regions). Unless we have additional information about the bidirectional reflectance, the surface model chooses either a Lambertian or specular reflectance approximation for the forward model calculation. In order to arrive at a reasonable first guess for the retrieval of land surface emissivity, or where appropriate, the bidirectional reflectance for a target surface scene, we use an up-to-date estimate of the seasonal land cover for the latitude and longitude of each pixel in a given nadir view. Since the footprint of an individual pixel is approximately 0.5×5 km, a database with spatial resolution of order 1 km (or 32 arcseconds) is sufficient. The database of land cover characteristics with 1-km resolution is described in the TES Level 2 ATBD Appendix [7].

2) RT for the Solar Contribution: Extraterrestrial solar radiance contribution to the TES observed radiance can be significant in the 2000–3050 cm^{-1} spectral region. Therefore, modeling of the solar contribution can be important for the daytime retrieval of molecules such as CO. In order to accurately model the impact of the solar radiation on the observed radiances, the solar source function of Kurucz [15], [16], shown in Fig. 6, is used in the forward model. It is the result of a radiative transfer calculation based upon solar measurements, including those of ATMOS [17], and includes a spatial integration over the solar disk. The Kurucz source function has a resolution of 0.0040 cm^{-1} at 2000 cm^{-1} and 0.0061 cm^{-1} at 3050 cm^{-1}, but for TES the spectra are interpolated and stored on the operational monochromatic frequency grid.

For RT calculations using the solar source function, the proper Doppler shifts between the scattering medium (nadir view) and the sun (due to Earth's rotation and orbit) and a radiance adjustment for the distance of the Earth to the sun must be applied to the spectrum. Initially, we have assumed a static solar source function, but we may need to include the effects of the solar cycle. Treatment of these effects involves minimal computation time.

The solar contribution in (7) can be written as

$$L_s = R_{\text{BRDF}}(\theta_{\text{sat}}, \theta_s)\, J_s \mathcal{T}_{0,\infty}(\theta_s)\, \mathcal{T}_{0,\infty} \tag{14}$$

where J_s is the extraterrestrial solar irradiance from Kurucz, $\mathcal{T}_{0,\infty}(\theta_s)$ is the atmospheric transmittance at the solar zenith angle θ_s, and $R_{\text{BRDF}}(\theta_{\text{sat}}, \theta_s)$ describes the scattering from the surface into the satellite direction. Experience with HIS spectra suggests that, under solar conditions, there is almost always some solar scattering due to atmospheric clouds and aerosols in addition to the scattering from the surface. The present approach for the limb observations is to remove spectra that are strongly contaminated by solar scattering in the 2000–3050 cm^{-1} spectral domain, but appropriate methods may be applied to extract as much information as possible for species optically active in this region [18] if strong aerosol conditions exist. The RT model to handle scattering effects more completely has been prototyped and tested using LBLRTM and has the capability to treat solar scattering in the single-scattering approximation at each layer given a profile of scatterers and their optical properties. The method of calculation is to use an effective secant for the solar path in each layer, thus making use of the optical depth calculation being done for the upwelling atmospheric radiation.

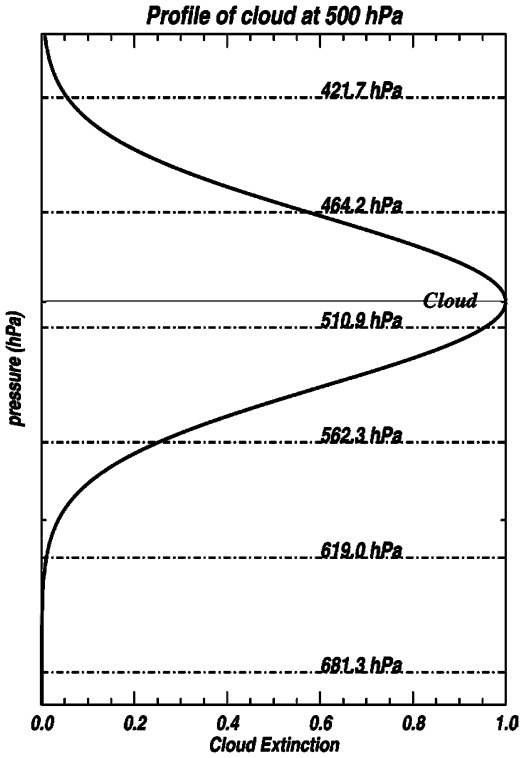

Fig. 7. Vertical profile of cloud extinction for a cloud at 500 mb.

3) RT for Clouds and Aerosols: The capability to address the radiative effects of aerosols and clouds in the forward radiative transfer model is an important issue for TES. Since clouds and aerosols introduce scattering into the RT problem, the increase in complexity for a full multiple-scattering approach is prohibitive for the present calculation. For a homogeneous layer, the clouds (or aerosols) are characterized by a scattering coefficient, k_s, and a single-scattering albedo, $\omega = k_s/k_a + k_s$, where k_a is the absorption coefficient of the scatterer. The scattering coefficients and single-scattering albedo are a slow function of frequency and may be characterized with a sampling grid of order 25 cm^{-1}. The approach that has been adopted is to characterize the effects of clouds with an effective cloud optical depth, defined and retrieved on the spectral grid appropriate to the variation of k_s and ω.

The approach described here has been developed and validated through simulation. Simulated spectral radiances were obtained at the satellite for a series of single layer cloud cases ranging over cloud type, cloud optical thickness, and cloud altitude using an accurate multiple-scattering code, CHARTS [19]. Through this method it has been established that the retrieval of molecular profiles, e.g., ozone, is robust for cloud optical thicknesses below one with degradation for higher optical thicknesses [20].

For this approach to the cloud problem, both the forward model state vector and the retrieval vector include an effective cloud height and effective cloud optical depth elements over the frequency range of interest. The distribution of the effective cloud absorption as a function of $\log(P)$ is shown in Fig. 7 by the relation

$$\tau_{\text{cld}}(\nu) = [k_{\text{cld}} l_{\text{cld}}]_\nu \exp\left[-\left(\frac{\ln P - \ln P_{\text{cld}}}{0.1}\right)^2\right]. \quad (15)$$

The quantity $[k_{\text{cld}} l_{\text{cld}}]_\nu$ is treated as a single quantity in both the forward model and the retrieval, and represents the effective absorption of the cloud including the effect of the photon path length, l_{cld}, due to the scattering in the cloud.

The vertical extent of the cloud is described by the difference of the upper and lower 1/e points above and below the center pressure. This corresponds to a geometric cloud thickness of ~ 1 km (FWHM) at all altitudes. As the opacity of the cloud increases to large values, the cloud takes on the characteristics of a black body with extensive multiple scattering at the upper boundary. The values of $[k_{\text{cld}} l_{\text{cld}}]_\nu$ should have little spectral content under this condition. The method adopted here is only applicable to single level clouds. More complicated cloud fields are not yet handled for TES retrievals.

For the limb, the clouds act as a lower boundary, in general spatially inhomogeneous. Stratospheric aerosols can be an important consideration in the limb, particularly for atmospheres affected by volcanic eruptions. The method described above for clouds in the troposphere is expected to be adaptable for aerosols in the stratosphere.

D. Instrument Line Shape Spectral Convolution and Apodization

In order to compare with the measured spectra, the calculated monochromatic spectra are convolved, or smoothed, with the instrument line shape (ILS) function. This convolution is described as

$$L_C(\nu) = \int_{-\infty}^{\infty} \Phi(\nu - \nu') L_M(\nu') d\nu' \quad (16)$$

where L_M and L_C are the monochromatic and convolved spectral radiances respectively, and Φ is the ILS function, which for an ideal FTS is a sinc function.

An efficient way of performing the convolution is to multiply the Fourier transforms of the L_M and Φ and then transform the result back to the frequency domain. This method directly simulates the operation of an FTS. The monochromatic radiances are transformed into an interferogram, apodized, and transformed back to obtain the convolved spectra.

The spectral range for L_M (the integration boundaries) calculated in the forward model is extended beyond the range of L_C. Study shows that this extension should be over 160 sinc halfwidths so that the error in L_C due to this truncation becomes insignificant [21]. In cases where microwindows are used for retrievals, this extension of the monochromatic spectra can make the forward model calculations more computationally expensive. For example, a $\pm$6-cm^{-1} extension is needed for TES nadir calculations. Norton–Beer apodization [22] is used to reduce this frequency extension. For the general case, 160 halfwidths corresponds to a sinc function amplitude decrease of 0.0035. Table III lists the spectral resolutions and the minimum extensions for L_M to derive L_C based on four different apodizations.

Although the line shape is asymmetric due to the off-axis geometry of the TES detectors [23], this effect was not observable above the noise level in averaged, high-resolution gas cell spectra taken during instrument calibration [24]. Therefore, we do not need to model this effect in Level 2. A sinc function corresponding to the maximum optical path difference (max

TABLE III
RESOLUTION AND POSSIBLE FORWARD MODEL EXTENSION VALUES

Apodization Case	Resolution Factor	Nadir Resolution (cm^{-1})	Nadir Extension (cm^{-1})	Limb Resolution (cm^{-1})	Limb Extension (cm^{-1})
None (box function)	1.0	0.07143	6.0	0.01786	1.5
Norton-Beer Weak	1.2	0.08571	3.36	0.02143	0.84
Norton-Beer Medium	1.4	0.10000	1.44	0.02500	0.36
Norton-Beer Strong	1.6	0.11429	0.48	0.02857	0.12

OPD) suffices for the instrument line shape. Interferogram self-apodization due to off-axis detectors is corrected in L1B for high-resolution spectra [25], [26]. Applying Norton–Beer apodization to the L1B spectra mitigates off-axis asymmetries, as well as other frequency grid interpolation errors. As discussed above, apodization is applied to the forward model in order to minimize the frequency range needed for the monochromatic calculation, and must therefore be applied to the L1B spectra as well.

E. Field-of-View Spatial Integration

The TES forward model derives the effective radiative response of a pixel at the satellite by performing a trapezoidal integration of the FOV function, with the representation of the radiance field provided by multiple rays originating at specified tangent points. The set of refracted path radiances, $L(\theta_k)$, is obtained by running the forward model over TES prescribed tangent pressure levels, $k = 0, \ldots, N_{\mathrm{ray}}$, with corresponding zenith angles at the TES focal plane, θ_k (see Fig. 2). The TES instrument spatial FOV function for detector d, $R_{\mathrm{FOV},d}$ is stored on an angular grid θ_j, $j = 0, \ldots, N_{\mathrm{FOV}}$ appropriate for the trapezoidal integration. The forward model radiances, $L(\theta_k)$, are interpolated to match the $R_{\mathrm{FOV},d}$ grid using a four-point Lagrange method for unequally spaced points with continuous first derivatives and are then integrated with $R_{\mathrm{FOV},d}$ to obtain the effective radiance at the detector. For the top and bottom rays, three-point Lagrange interpolation is used. The calculated radiance for detector d at the satellite L_{sat} is given as

$$L_{\mathrm{sat}}(\theta_d) = \sum_{j=0}^{N_{\mathrm{FOV}}} L(\theta_j) R_{\mathrm{FOV},d}(\theta_j - \theta_d) \Delta\theta_j \tag{17}$$

where $\theta_d = \theta_p + \Delta\theta_d$; θ_p is the instrument pointing angle, which corresponds to the TES boresight; $\Delta\theta_d$ is the fixed angular difference between this point and the center of detector d, and $\Delta\theta_j = 1/2(\theta_{j+1} - \theta_{j-1})$.

To implement this radiance integration efficiently, we switch the order of interpolation and summation over FOV angles to obtain frequency-independent coefficients that are then applied to the ray radiances (refer to the TES Level 2 ATBD for more details [7]). This allows a significant portion of the FOV calculation to be performed after ray tracing, when the ray angles are available, but before the RT, i.e., without frequency dependence.

The analytic partial derivatives of L_{sat} with respect to θ_p for each detector is calculated at little computational cost. These Jacobians are used for the retrieval of the pointing angle.

III. TES ABSORPTION COEFFICIENT TABLE GENERATION

The strategy for the computation of the optical depths used in the RT calculation is a critical consideration for the forward model. For TES, the decision was made to perform the radiative transfer with the highest monochromatic accuracy attainable without resorting to accelerated schemes that have the potential to add algorithmic forward model error. Precalculated absorption coefficient files (ABSCO tables) are utilized to circumvent the computational cost of a line-by-line calculation. This lookup table method has been used in the past for such instruments as High Resolution Infrared Radiation Sounder (HIRS) [27].

The optical depth (OD) along the line of sight for a given layer l is calculated as

$$\tau(\nu)_l = \sum_m u_{m,l} k_m\left(\bar{P}, \bar{T}, \nu\right) \tag{18}$$

where the sum is over species, $u_{m,l}$ is the layer molecular amount for absorber m, and $k_m(\bar{P}, \bar{T}, \nu)$ is the absorption coefficient for molecule m. $u_{m,l}$, $\bar{P}$, and $\bar{T}$ are calculated in the ray-trace and path integral step. The $k_m(\bar{P}, \bar{T}, \nu)$ for the molecular species are precalculated at fixed pressure and temperature grids and stored in the absorption coefficient files.

For TES, the absorption coefficients have been developed on a temperature/pressure grid that enables the calculation of optical depths with accuracy effectively equivalent to that provided by a line-by-line calculation. The accuracy of the optical depths and resulting spectral radiances is directly related to the accuracy of the line-by-line model used for the computation of the absorption coefficient table.

The line-by-line code used to generate the TES spectral absorption coefficients is a version of LBLRTM adapted to specifically address TES accuracy requirements. The LBLRTM model has been extensively validated against both upward and downward radiance observations taken by a number of different instruments; an example is provided in Section V. Since LBLRTM is run off-line to generate the absorption coefficients for the ABSCO tables, the emphasis is on accuracy, not computational efficiency. In particular, LBLRTM includes the very accurate Armstrong [28] Voigt line shape option based on a linear interpolation between precalculated Voigt functions.

The absorption coefficients for a given molecular species as a function of pressure, temperature, and frequency are precalculated and stored utilizing the best spectral line information available for that species. The pressures for which the absorption coefficients are tabulated are the TES forward model layer effective pressures. An advantage of using fixed pressure levels bounding the TES forward model atmospheric layers is the ability to ignore the interpolation of species absorption coefficients in pressure at all layers except two: the layer nearest the Earth's surface in the nadir case, and the tangent layer in the limb case. For each effective layer pressure the absorption coefficients are calculated for 13 temperatures centered on the U.S. standard atmospheric temperature profile [29] at 10 K intervals. The total layer optical depth at a specified temperature is obtained as the sum of the layer optical depths for all the relevant species interpolated to the proper temperature.

In the case of water vapor, self-broadening causes a nonlinear dependence on the optical depth with respect to water vapor concentration that must be taken into account. The H_2O volume-mixing ratio (q) is therefore another variable in the ABSCO tables for tropospheric H_2O. Since the dependence of the H_2O absorption coefficient on q is nearly linear for a given temperature and pressure, we use linear interpolation/extrapolation in q to calculate the H_2O absorption coefficient for the associated three temperature values. The two tabulated q grids are for extremely dry air, $q_{\rm dry} = 10^{-8}$, and for 90% of the saturation $q_{\rm sat}$ at the given temperature and pressure grid, $q_{\rm wet} = 0.9q_{\rm sat}$.

In general, by comparison to real time line-by-line calculations of ABSCO, the advantage of table lookup is to greatly speed up the calculation of the required spectral optical depths. The effect of interpolations (temperature, pressure, and tropospheric q) on TES retrievals was examined thoroughly. Studies for both the nadir and limb cases have shown that compared to the spectral radiance calculated by line-by-line code, the radiance differences are less than 0.05% in the nadir and less than 0.1% in the limb [7]. A significant advantage of the ABSCO approach is that the accuracy of the absorption coefficient calculation is not limited in any way by computational cost considerations. In addition, the spectral absorption coefficients are readily amenable to empirical adjustment as atmospheric measurements may suggest for improved retrievals.

Similar to the table lookup strategy used for the absorption coefficients for the lighter molecules with high spectral content, the cross-section absorption coefficient table for heavier molecules is obtained: 1) from a line-by-line calculation on the predefined pressure and temperature grid (e.g., for HNO3) or 2) interpolation of laboratory measurement onto TES P/T table grids (e.g., the CFCs).

A. Databases for TES Absorption Coefficients

1) Line Parameters: The accuracy of the forward model is critically dependent on the line parameters used for the generation of the ABSCO tables. The HITRAN 2000 line parameters [30] with updates available through 08/2003 (last update 09/2001) provide the basis for the initial version of the TES ABSCO tables. The numbering of the species, the format and definition of the parameters including the vibrational state designations are consistent with the HITRAN 2000 compilation. The HITRAN 2004 parameters [31] did not become available in time for the requisite validation and inclusion in the initial TES forward model. However, we did have access to some of its important updates for the HITRAN 2004, included as described below. Other improved lists will be incorporated in the future as needed.

The spectroscopic line parameters are evaluated under the aegis of a number of atmospheric measurement programs, most particularly the ARM program. The TES database is a customized subset of these validated line parameters. It should be emphasized that the AURA instruments utilize spectral domains including the microwave (MLS), thermal infrared (TES and HRDLS) and ultraviolet (OMI). A concerted effort has been made in this work to retain consistency across the relevant spectral domains, particularly with respect to the ozone line parameters. The TES line parameter database (tes_v_1.2) is publicly available to the research community (http://rtweb.aer.com/).

In Table IV, we provide a brief overview of the TES line parameter sources for selected key species. Also indicated are estimated percent uncertainties for the line intensities and widths of the strongest transitions. It should be noted that the weaker transitions are expected to have errors greater than those for the stronger transitions.

In the following section we discuss the line parameters for selected important species.

a) Water vapor: It should be noted that the significant improvements in atmospheric radiative modeling are due in considerable measure to recent improvements in water vapor spectroscopy by Toth [32], which are included in HITRAN2000 updates (01_HIT01.par). The water vapor line parameters used by TES are effectively the same as HITRAN 2004 in the spectral region relevant to TES.

To address issues of isotopic differentiation in the atmosphere, the water vapor line parameters have been separated into three files: 1) all water vapor isotopomers; 2) nondeuterated isotopomers; and 3) deuterated isotopomers (e.g., HDO). The strengths for HDO lines in the latter set have been scaled by the appropriate deuterium abundance such that the associated volume mixing ratio for deuterium is with respect to dry air.

b) Carbon dioxide: The line parameters of CO_2 have been taken from HITRAN 2000. The values for the strengths are based on the 1992 work of Rothman *et al.* [33], [34]. Line coupling for carbon dioxide Q-branches plays a significant role in the spectral absorption [35]. The line coupling parameters for Q-branches in the 612–796 $\rm cm^{-1}$ region are consistent with the HITRAN 2000 line parameters and are updated values of those described in the work of Hoke *et al.* [36]. The carbon dioxide line coupling parameters from 1930–2130 $\rm cm^{-1}$ are taken from Strow [37]. Improvements to these parameters will be incorporated as new results become available.

c) Ozone: The positions, intensities and broadening parameters for ozone in the TES spectral region are those of Wagner *et al.* [38]. The rationale for using this set involves a number of considerations: 1) The retrieval of tropospheric ozone from space is highly dependent on the accuracy of the widths. The halfwidths, obtained by extensive measurement, are significantly different from HITRAN 2000 and give better agreement in atmospheric validations; and 2) These line parameters are being used for the MIPAS forward model [39].

With respect to the line strengths, accuracy of the infrared values still remains uncertain in the range of 3% [40], [41]. Further analyses making simultaneous measurements in the ν_3 band region with microwave and/or ultraviolet Hartley band measurements are needed to resolve the discrepancies in the ν_3 band strength.

d) Carbon monoxide: The carbon monoxide line positions and intensities for TES are those from the HITRAN 2000 database. The broadening coefficients are based on the work of Zou and Varanasi [42] for air-broadened widths, pressure shifts and temperature dependence of widths. The actual TES linelist was compiled by Smith *et al.* [43]. For the widths, a fourth-order polynomial in the rotational quantum number

has been applied to all transitions (ground state, hot, isotopic bands) to achieve improved consistency and accuracy. A similar approach was used for HITRAN 2004.

e) Methane: The line positions and intensities for methane are taken from the "2001 update" described by Brown *et al.* [44] as a total replacement of the methane parameters in HITRAN 2000. The new methane database contains transitions from the ground state for all the fundamentals of all three isotopomers. In addition, predictions are included for ten hot bands of $^{12}CH_4$ and $^{13}CH_4$ in the 504–2077 cm^{-1} region and for 15 hot bands of $^{12}CH_4$ from 2341–3370 cm^{-1}. For the most part, the width coefficients for CH_4 are values estimated by averaging empirical measurements of the strongest bands according to the quantum numbers J in the manner described by Brown *et al.* [44]. Some direct measurements of widths are inserted for over 1000 of the strongest transitions. While the accuracy of the measured widths is thought to be 3% and better, the J-averaged widths are accurate to 20% at best. Measured pressure-induced shifts in line positions are inserted for several hundred transitions but for most of the lines the shifts are estimated using the value of the line position as a scaling factor. Following the creation of the "2001 update" version, the investigators using MIPAS data noticed that some pressure-broadened coefficients were incorrectly inserted; corrections were made for some 130 transitions, as described by Flaud *et al.* [39]. The TES (tes_v_1.2) methane list below 1600 cm^{-1} is the same as the MIPAS 2003 methane compilation; however, this final correction was not included in HITRAN 2004. It should be noted that line coupling parameters for the methane Q-branch at 1305 cm^{-1} are anticipated [45] but are not yet available.

f) Nitric acid: The line parameters for nitric acid are those used by MIPAS and subsequently adopted for HITRAN 2004. The improvements in the MIPAS line parameters provide greater consistency within the TES spectral region, and with the spectral regions associated with other instruments [39], [46].

g) Formic acid: Updated line parameters provided by Perrin *et al.* [47] significantly improved accuracy in the ν_6 band located at 1105 cm^{-1}. These parameters have been used for the TES absorption coefficients and are also included in HITRAN 2004.

2) Isotopes: In general, the spectral line intensities used by TES are weighted by the natural terrestrial isotopic abundance of the isotopologue as in HITRAN. The selection of a particular molecular species includes the contribution of all associated isotopes at their respective natural terrestrial abundances independent of altitude. To study the dependence of a given isotope with altitude (e.g., HDO) that isotope is treated as a separate molecular species.

3) Cross-Sections: For heavy molecular species such as chlorofluorocarbons (CFCs), hydrochlorofluorocarbons (HCFCs), and SF_6, spectral absorption cross-sections measured at atmospheric conditions are required [38], [48]. This is essential, since the small rotational constants, low vibrations and strong hot bands of such molecules preclude complete modeling of the individual line transitions. The 1986 and 1992 editions of the HITRAN compilation introduced temperature-dependent cross-sections but neglected the effect of pressure broadening [49]–[52]. More recently, pressure-temperature cross-sections sets have become available [53]–[55].

TABLE V
INFRARED CROSS-SECTION DATA FOR TES

Molecule	Wavenumber Range (1/cm)	Temperature Range (K)	Pressure Range (torr)	Number of P,T sets
CCl_4	770-812	208-297	8-760	32
CFC-11 (CCl_3F)	810-880	190-296	8-760	55
	1050-1120	190-296	8-760	55
CFC-12 (CCl_2F_2)	810-965	190-296	8-760	51
	1040-1200	190-296	8-760	51
HCFC-22 ($CHClF_2$)	760-860	216-294	40-760	7
SF_6	925-955	216-295	25-760	7
CF_4	1250-1290	180-296	8-760	54
HFC134a (CFH_2CF_3)	1000-1350	253-287	0	3

Note: $ClONO_2$ and N_2O_5 cross-sections will be added, as they are significant for limb-viewing observations.

TABLE IV
LINE PARAMETER SOURCES FOR KEY TES SPECIES

Species	Sources	Estimated Uncertainties (%)	
		Intensity	Widths
H_2O	Toth [32], Rothman et al.[30]	3	3
CO_2	Line Parameters: Rothman et al. [33], [34] Line-coupling: Hoke et al. [36], Strow et al. [37]	3	2
O_3	Flaud et al. [39], Rothman et al. [31]	4	5
CO	Rothman et al. [31]	2	1
CH_4	Flaud et al. [39]	3	3→20
HNO_3	Flaud et al. [39], Rothman et al. [31]	7	50

The absorption cross-section, κ_v, is defined as

$$\kappa_\nu = \frac{(-ln\mathcal{T}_\nu)}{nL} \tag{19}$$

in terms of the spectral transmittance $\mathcal{T}$ at wavenumber ν, temperature T and pressure P, of column density n along an optical path of length L (cm). It is presented at several (T, P) combinations representing atmospheric layers given in commonly tabulated atmospheric models as well as conditions encountered in the polar regions.

Table V shows the datasets that have been adapted for TES, from an updated set of measurements provided by Varanasi [56]. These form an extension of the cross-sections of CFC-11, CFC-12, HCFC-22, and SF_6 provided by Varanasi for 1996 HITRAN [57]–[60] and also include CF_4. The cross-sections of CCl_4 listed in 1996 HITRAN, which originate from the work of Orlando *et al.* [61], have been replaced for TES by those of Varanasi.

For the purpose of TES codes, the cross-sections that are originally given at different spacing (chosen according to resolution and pressure) were interpolated to a constant grid of 0.0025 cm^{-1}. A special P-T interpolation was devised for conditions different from the laboratory data. Table V shows the data sets prepared on the TES system and TES Level 2 ATBD describes the P-T interpolation program XSFINT. The data are stored in HITRAN format (i.e., as separate files for each individual molecule).

The rest of the molecular cross-sections sets are taken from the 1996 HITRAN database, which, compared to 1992 HITRAN, provides an update for $ClONO_2$. In addition to the $ClONO_2$ ν_4 line parameters, new cross-sections for the $ClONO_2$ in the 1265–1325 cm^{-1} region at 201, 211, and 222 K are available from 1996 HITRAN, as provided by Orphal *et al.* [62].

The increased use of hydrofluorocarbons (HFCs), which are expected to replace CFCs and HCFCs in many applications in order to reduce the deleterious effects of released chlorine on the atmospheric ozone layer, will add another absorber in the IR "window" region, 8–12 μm. Cross-section data for a number of HCFCs have become available [63], [64]. More recently, Smith *et al.* [65] determined the cross-sections of HFC-134 (CHF_2CHF_2) and HFC-143a (CF_3CH_3). All of these data are already available on the GEISA database [66] and will be incorporated into HITRAN. We also prepared in TES format the cross-sections of HFC-134a (from Clerbaux *et al.* [63]), which is considered as one of the most popular HCFCs.

4) Aerosols: The HITRAN 2000 compilation contains auxiliary tables in ASCII for various atmospheric particles. The index of refraction tables include water and ice (the composition of cloud particles), aqueous sulfuric acid (the composition of volcanic aerosols), and nitrate acid trihydrate and aqueous HNO_3/H_2O (possible compositions of polar stratospheric clouds). The tables have individual wavenumber ranges, increments, and data formats. A description of the individual files is reported in Rothman *et al.* [30]. Note that most of the available measurements were obtained only at room temperature.

The emission measurements obtained by TES will display enhanced radiances due to the scattering and absorption by aerosol particles. As is well known, sulfate aerosol injection into the stratosphere after a major volcanic eruption will greatly increase radiance levels. At such times, strong aerosol bands appear throughout infrared limb spectra [18].

5) MT_CKD Continuum: A new continuum model has been developed for TES that includes continua due to water vapor, carbon dioxide, oxygen, and nitrogen. The water vapor continuum [2], [67], [68] and carbon dioxide continua are developed and utilized such that when the continuum contribution is added to the line-by-line component, agreement with observation is achieved. These continua have slow spectral dependence and known thermodynamic scaling. The continua for oxygen [69] and nitrogen [70] are due to collision-induced effects resulting from collisions with the respective molecule and the molecules comprising the air.

The water vapor continuum plays an important role in atmospheric radiative transfer providing increased opacity between spectral lines over the full spectral region from the microwave to the visible. The continuum is important to the physical solution of the inverse problem, the remote sensing of atmospheric state to retrieve temperature, water vapor, and trace species profiles as well as surface properties. There are two components to the continuum: the self-broadened continuum (C_s), dependent on the square of the partial pressure of water vapor, and the foreign-broadened continuum (C_f), dependent on the product of the water vapor partial pressure and the dry air pressure. As a consequence the self-broadened continuum tends to be more important in the lower troposphere while the foreign-broadened continuum tends to be more important in the middle to upper troposphere.

As a result of more stringent accuracy requirements for remote sensing applications and with the availability of improved atmospheric observations, an entirely new water vapor continuum formulation has been developed. The MT_CKD continuum is based on a new formulation in which the self and foreign continuum models are each based on the contributions from two components: a collision induced component and a line shape component. This change in perspective has resulted from the difficulty in developing a line shape formalism, such as in CKD, based on sound physics that explains the magnitude of the increased absorption in the intermediate line wing over that provided by the impact approximation. The two components in MT_CKD are applied consistently to all water vapor lines from the microwave to the visible, and the results summed to obtain self and foreign continuum coefficients from 0–20 000 cm^{-1}. Eight and seven parameters are needed to specify the two components for the self and foreign continua, respectively, which are sufficient to generate the entire continuum spectrum over this spectral domain. The ratio of the self-continuum at 296 K to that at 260 K has been kept the same as in the CKD model. The only temperature dependence for the foreign continuum arises from the radiation term as with CKD. The MT_CKD model (as with CKD) should be regarded as a semiempirical model with strong constraints provided by the known physics. The principal consequences for remote sensing are with respect to the foreign continuum, important in the upper troposphere for the retrieval of water vapor and for the background spectral radiance for retrieval of trace species including NO. Examples of the role of the continuum for atmospheric observations may be found in Shephard *et al.* [71], Shephard [72], Clough [10], and Mlawer [73].

IV. Jacobians

The sensitivity of the spectral radiance at the satellite to perturbations of retrieved parameters is the Jacobian matrix, $\mathbf{K}$. In general, $\mathbf{K} = \partial\mathbf{F}/\partial\mathbf{x}$, where $\mathbf{F}$ is the forward model radiance and $\mathbf{x}$ represents a retrieved parameter, such as temperature at level l. In our retrievals, we cannot assume we are close to a linear solution. Therefore, Jacobians are recalculated for each iteration in a retrieval, using updated parameters.

Evaluating Jacobians using a finite difference method is straightforward. For example, $\mathbf{K}$ can be calculated as $[\mathbf{F}(\mathbf{x}+\Delta\mathbf{x}) - \mathbf{F}(\mathbf{x})]/\Delta\mathbf{x}]$, where $\Delta\mathbf{x}$ is a small perturbation of parameter $\mathbf{x}$. However, the computation can be expensive if not optimized, and the accuracy of the derivatives is more prone to numerical error and nonlinear contributions. For these reasons, we compute analytic Jacobians for operational retrievals and retain the finite difference method for validating analytic Jacobians.

For atmospheric temperature and gas concentration, the analytic derivative of the radiance at the satellite for a change in parameter x_l at level l is more conveniently written in terms of associated layer quantities, so that we have

$$\frac{\partial L_{\text{sat}}}{\partial x_l} = \sum_j \frac{\partial L_{\text{sat}}}{\partial \overline{x}_j} \frac{\partial \overline{x}_j}{\partial x_l} \tag{20}$$

in which x_l is an element of the retrieval vector associated with level l and $\overline{x}_j$ is the associated layer quantity for layer j. The parameter x may be mixing ratio, log mixing ratio or temperature in this context. The $\partial\overline{x}_j/\partial x_l$ terms are independent of

wavenumber and are calculated along with the layer quantities during the ray-tracing procedure.

For the layer quantities, it is useful to separate the Jacobian calculation into partial derivatives with respect to layer total optical depth (τ_l) and Planck function (B_l) via the chain rule

$$\frac{\partial L_{\rm sat}}{\partial \overline{x_l}} = \frac{\partial L_{\rm sat}}{\partial \tau_l}\frac{\partial \tau_l}{\partial \overline{x_l}} \tag{21}$$

for gas species, and

$$\frac{\partial L_{\rm sat}}{\partial \overline{T_l}} = \frac{\partial L_{\rm sat}}{\partial \tau_l}\frac{\partial \tau_l}{\partial \overline{T_l}} + \frac{\partial L_{\rm sat}}{\partial B_l}\frac{\partial B_l}{\partial \overline{T_l}} \tag{22}$$

for layer temperature $\overline{T_l}$. This approach has the advantage of relatively simple expressions for the derivatives of τ_l with respect to log mixing ratio and temperature. It is also compatible with the modularity designed into our code where quantities associated with optical depth are computed first to determine whether they can be reused from one ray calculation to the next, while quantities associated with layer to layer radiative transfer are used locally in different functions. The expressions for each of the above terms are given in detail in TES Level 2 ATBD Appendix and summarized here.

The partials of radiance with respect to layer total optical depth have straightforward recursion relationships and can be computed concurrently with the radiance and transmittance terms in the RT calculation.

The partials of optical depth with respect to mixing ratio are very simple for all gas species except H_2O: $\partial\tau_l/\partial \ln \overline{q}_{l,m} = \tau_{l,m}$, i.e., the partial of total layer optical depth with respect to log mixing ratio for species m is just the layer optical depth of species m. Partials of optical depth with respect to water vapor mixing ratio have additional terms for line self-broadening, continuum, and integrated path amount dependence, which cannot be neglected and are taken into account in the calculations.

The temperature Jacobians include terms for gas species line absorption, continuum absorption, dependence of the integrated path amount and Planck function dependence. (When the linear-in-tau approximation [10] is used, the temperature dependence of the effective Planck function replaces $\partial B_l/\partial T_l$.) For absorption coefficient tables, the temperature partials for species line absorption are a straightforward differentiation of the coefficients using three-point Lagrange interpolation in temperature.

When the surface or a cloud boundary is modeled, surface temperature Jacobians are computed from the surface Planck function term. If surface or cloud emissivity is retrieved, Jacobians are computed for parameters on the tabulated grid for the emissivity first guess (usually 10 $\rm cm^{-1}$). At present, we use a simple linear interpolation between grid points, with Jacobians that use the same interpolation coefficients.

For limb measurements, we also retrieve a single pointing angle corresponding to the instrument optical axis in order to determine the relative alignment of the detector FOV functions to the ray radiances computed from tangent pressures on the fixed pressure grid. The Jacobian for this pointing angle is generated along with the FOV integration by differentiating the coefficients for the angular four-point Lagrange interpolation.

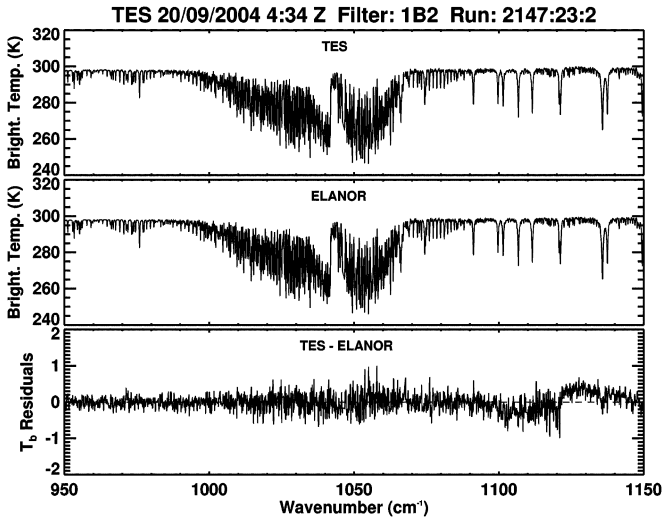

Fig. 8. Top panel is a preliminary TES nadir observation (calibration is currently being refined). The middle panel is the corresponding ELANOR forward model calculation, and the bottom panel is a residual plot between the observation and the calculation.

V. Forward Model Results

In order to demonstrate that the TES forward model calculations can represent the TES observations a preliminary TES measurement from an early global survey is provided, refer to Fig. 8. The TES nadir viewing observation took place on September 20, 2004 over water at 133.8° longitude and 20.9° latitude (run 2147, sequence 23, scan 2). All of the 16 nadir viewing pixels were averaged together reducing the random instrument noise. The retrieved temperature, water vapor, and ozone profiles were used as input into ELANOR forward model calculations. The retrieved parameters are used because the purpose of this example is not to perform a true validation, but rather just an example to show that ELANOR can reproduce the TES observations. The small residuals (TES -ELANOR) in Fig. 8 show that the model represents the observations taken by TES.

The task of validating the forward model at the accuracies required to meet the objectives of TES is not a simple matter. For the forward model radiances, the absolute accuracy objective is 0.5% or better, yet very few of the line parameters are known to this accuracy. The perspective of validating the forward model performance through validation of the retrieval products has significant limitations. A common approach, the use of sondes for temperature, water vapor, and ozone has the inherent problems of temporal and spatial sampling. In addition, the accuracy of the sonde measurements themselves may not be sufficiently accurate. For water vapor, sondes typically exhibit peak-to-peak errors of 15% in the column with larger errors in the upper tropospheric humidity [74].

The TES forward model is continuously validated against LBLRTM through numerous regression tests. LBLRTM is validated extensively against both upward and downward radiance observations taken by a number of different instruments over a wide range of atmospheric conditions [71], [72], [75], [76]. In general, the spectral residuals from these validations have been acceptably low for the purposes of TES. However, there are

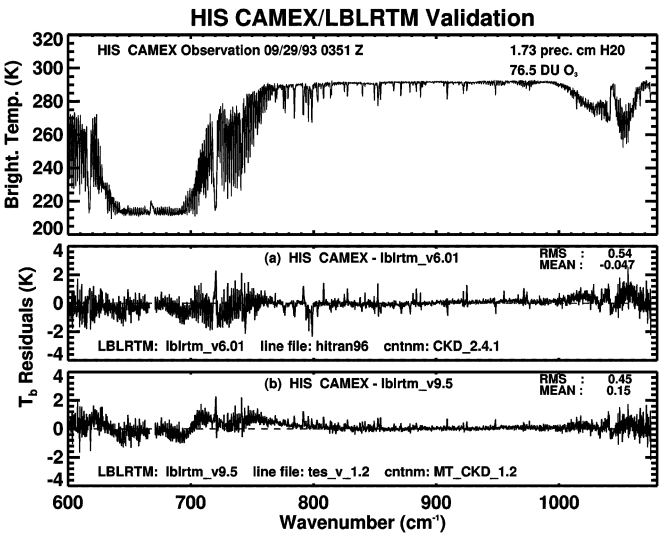

Fig. 9. Top panel contains the HIS observations. The middle and bottom panels are residual plots of (a) HIS CAMEX -LBLRTM_v6.01 with HITRAN96 spectral line parameters and CKD_2.4.1 continuum. (b) HIS CAMEX -LBLRTM_v9.5 with tes_v_1.2 spectral ine parameters and MT_CKD_1.2 continuum. In the bottom panel, the variation about the local spectral mean has been reduced to the point that errors in the vertical temperature profile are apparent at the 1 K level.

spectral regimes for which continuing line-by-line model evaluation and improvement is required, including the 650–800 cm^{-1} carbon dioxide region [77], the methane region at 1300 cm^{-1}, and the carbon dioxide line coupling in the 2076 cm^{-1} spectral region. The magnitude of the residuals is such that errors including the specification of atmospheric state, spectroscopic line parameters, and instrument function are of similar order as those of the model errors, presenting a significant challenge to forward modeling improvement.

As an indication of the current level of model performance for a portion of the longwave spectral region, we provide in Fig. 9 a radiance spectrum in equivalent brightness temperature obtained with the University of Wisconsin High-resolution Interferometer Sounder (HIS). The data were taken from the NASA ER2 aircraft during the 1993 Convection and Moisture Experiment (CAMEX) aircraft at an altitude of 20 km in a nadir view over the ocean. The resolution of the unapodized spectrum is 0.32 cm^{-1} (half-width at half-maximum). The absolute radiometric calibration is better than 1 K with the relative calibration better than 0.5 K. The bottom residual plot in Fig. 9 shows the difference between the HIS brightness temperature spectrum and an LBLRTM-calculated spectrum utilizing the TES line parameter database (tes_v_1.2). Despite the limitation that the atmosphere utilized for the validation was obtained from radiosonde data, which was neither cospatial nor cotemporal, the comparison is extremely good. The surface temperature and emissivity have been adjusted to minimize the brightness temperature differences in the atmospheric window region. The ozone residuals in the 980–1080 cm^{-1} region have been improved by utilizing a retrieved ozone profile obtained from the spectral data. The effects of heavy molecules including CCl_4, CFC11, and CFC12 have been taken into account as cross-sections in the calculation. Carbon dioxide line coupling effects in this region have been accounted for using the temperature-dependent first- and second-order coupling coefficients of Hoke *et al.* [36]. The spectral residuals around 668 cm^{-1} have been omitted as there is a calibration issue due to strong CO_2 emission in the instrument. The regularly spaced spectral residuals in the 600–650 and 700–760 cm^{-1} regions are an active area of research as this is the region used for temperature retrievals by many passive remote sensing sensors. The residuals are associated with carbon dioxide and are due to remaining issues with carbon dioxide line parameters. Smilar residual signatures are also seen in validations with other sensors (i.e., Scanning-HIS AFWEX spectra) [71]. A contribution to the spectral residuals undoubtedly results from errors in the atmospheric temperature and humidity profiles. For example, the residual envelope in the ν_2 CO_2 region (600–800 cm^{-1}) is evidence of the atmospheric temperature profile not representing the true state of the atmospheric temperature field. It must be noted that such detailed analysis can only be performed because of the high quality of the spectral radiance data in terms of the photometric calibration, the noise and the spectral calibration.

VI. Future Forward Model Enhancements

A. Non-LTE

The non-LTE capability is still under active investigation. Although no species with non-LTE behavior is a standard TES product, it is desirable to have capability to treat non-LTE behavior for special investigations. Under certain conditions, the radiating system may not be in local thermodynamic equilibrium for which the translational, rotational, and vibrational state distributions are characterized by a single temperature. In particular, nitric oxide (NO) and carbon dioxide (CO_2 ν_3) exhibit nonthermal radiative behavior, particularly in the presence of solar excitation. This emission can be a significant fraction of the total measured signal. To account for non-LTE, the forward model must be able to accept the populations of the individual vibrational levels. The algorithm for the calculation of non-LTE radiances is based on LBLRTM, with the description provided in the TES ATBD Appendix [7], and requires the non-LTE state populations for the TES spectral measurements. The two approaches presently being explored to obtain these non-LTE state populations are: 1) estimate the populations of the excited states, using existing models and climatological temperature and solar irradiance values; and 2) retrieve the populations of the affected vibrational levels at all relevant altitudes, as well as the mixing ratio distribution.

B. Horizontal Inhomogeneity

At the limb, the path length through the tangent layer can be many tens of kilometers. Consequently, the assumption that the atmosphere is homogeneous in composition and physical state may not be valid. This is a challenging issue, therefore, the ensuing discussion reflects ongoing analyses with TES data. The approaches being investigated (in order) are as follows.

1) Ignore line-of-sight gradients in the forward model, retrieve a single profile from a single set of spectra, and include the effect in the error analysis (i.e., if a gradient exists, the residuals will increase).

2) Assume some known LOS gradients in the forward model. For temperature/pressure this can come from meteorological data. For constituents it can come from a first pass using method 1). This approach has been used by LRIR, LIMS, and ISAMS.
3) First perform a "nadir-type" retrieval (but with cold space rather than the Earth's surface as background) along the LOS. The weighting and contribution functions will be strongly peaked in the tangent layer, but this is where inhomogeneity will have most of its impact. Use the results (one for each pixel) as a first guess for the standard limb retrieval.
4) Retrieve the two-dimensional distribution (or at least a mean profile and a profile of the LOS gradient) from a single set of spectra. If horizontal inhomogeneity has a measurable effect on the radiances, then in principle there is information about it from which it might be retrieved. However this information might also alias into something else. Only numerical experiments can tell the difference.
5) Simplified tomography by sequential estimation. For example, consider successive profiles at the locations corresponding to three successive measurements. Call them A, B, and C in time order. Set up an *a priori* and use the B spectra to retrieve all three profiles jointly. The result gives the final retrieval for the A profile. The retrievals so far for B and C become *a priori* for the next cycle, and *a priori* for D, the next location, are obtained by a combination of, for example, climatology and extrapolation. Now use the C spectra to retrieve B, C, and D jointly. This gives the final retrieval for B and the C and D *a priori* for the next cycle. Repeat.

VII. Summary

The TES forward model has been described here in some detail outlining the implementation and methodology used to generate monochromatic radiance calculations with the accuracy and computational efficiently required for the retrieval of atmospheric constituents from TES measurements. Some of the model attributes described here, e.g., the treatment of clouds, have resulted from analyzing the TES data themselves. Validation of the forward model spectral radiances with TES measurements is highly dependent on the photometric accuracy of the TES radiances, now established to be at a satisfactory level through comparisons with AIRS and SHIS.

An important and continuing task of the TES forward model effort is the assessment and improvement of the forward model. At the level of accuracy required for the present application, this is a challenging task. For the accuracies in the spectral radiance measurements now being obtained from space, line parameters with accuracy better than 1% are required. Even in the laboratory, obtaining this level of accuracy for the range of thermodynamic conditions and path lengths required, e.g., water vapor measurements at 260 K, 500 hPa, and 1 km, has not been achieved. One commonly used and somewhat limited approach in the evaluation of forward model performance is the comparison of retrieved profiles with those provided by sondes or other *in situ* measurements, e.g., the comparison of retrieved water vapor profiles with those obtained with radiosondes. The problem with this approach is that although it provides an assessment of retrieval performance, it is critically dependent on the errors associated with the *in situ* measurements. These errors include spatial and temporal sampling errors and in the case of water vapor cited above, errors in the humidity measurements particularly in the upper troposphere, which may be as large as 50%. A second difficulty with this type of assessment is that little insight is provided with regard to the error sources. Again in the case cited, it is not clear whether the errors in the retrieved water vapor profile are due to errors in the temperature field or in the forward model parameters associated with water vapor. In our view, the extensive information associated with high-resolution spectral measurements has not been adequately utilized to assess and improve the forward model performance. For passive remote sensing, obtaining an accurate temperature field is the most critical task, as this field affects the radiances associated with the molecular species to be retrieved. Currently in this regard, the most serious limitation in the forward model are the errors in the carbon dioxide line parameters, particularly in the 600-800 cm^{-1} region. Our approach to addressing this problem will be the simultaneous retrieval of line parameter information and temperature profile for a range of cases, thus taking advantage of the high spectral resolution and extended spectral range of the radiance measurements. Measurements of upwelling radiance from TES, AIRS, SHIS, and of downwelling radiance from AERI at the ARM sites will be used for this purpose. Through this procedure we will achieve consistency between the ν_2 CO_2 bands (600-800 cm^{-1}) and the N2O and ν_3 CO2 bands (2000-2400 cm^{-1}). The key to forward model improvement is contained in the spectral residuals between the forward model calculation and the spectral radiance measurement.

Acknowledgment

The authors would like to thank E. Ustinov (JPL) for his earlier work. The authors would also like to thank the reviewers for their very constructive and helpful comments.

References

[1] R. Beer, T. A. Glavich, and D. M. Rider, "Tropospheric Emission Spectrometer for the Earth Observing System's Aura satellite," *Appl. Opt.*, vol. 40, pp. 2356–2367, 2001.
[2] S. A. Clough, M. W. Shephard, E. J. Mlawer, J. S. Delamere, M. J. Iacono, K. Cady-Pereira, S. Boukabara, and P. D. Brown, "Atmospheric radiative transfer modeling: A summary of the AER codes," *J. Quant. Spectrosc. Radiat. Transf.*, vol. 91, pp. 233–244, 2005.
[3] S. A. Clough, F. X. Kneizys, L. S. Rothman, and W. O. Gallery, "Atmospheric spectral transmittance and radiance: FASCOD1B," *Proc. SPIE*, vol. 277, pp. 152–166, 1981.
[4] K. Bowman, C. D. Rodgers, S. Sund-Kulawik, and J. R. Worden, "Tropospheric Emission Spectrometer: Retrieval method and error analysis," *IEEE Trans. Geosci. Remote Sens.*, vol. 44, no. 5, pp. 1297–1307, May 2006.
[5] S. A. Clough, C. P. Rinsland, and P. D. Brown, "Retrieval of tropospheric ozone from simulations of nadir spectral radiances as observed from space," *J. Geophys. Res.*, vol. 100, pp. 16 579–16 593, 1995.
[6] S. A. Clough, J. R. Worden, P. D. Brown, M. W. Shephard, C. P. Rinsland, and R. Beer, "Retrieval of tropospheric ozone from simulations of limb spectral radiances as observed from space," *J. Geophys. Res.*, vol. 107, no. D21, pp. 4589–4589, 2002.

[7] R. Beer, K. W. Bowman, P. D. Brown, S. A. Clough, A. Eldering, A. Goldman, D. J. Jacob, M. Lampel, J. A. Logan, M. Luo, F. J. Murcray, G. B. Osterman, D. M. Rider, C. P. Rinsland, C. D. Rodgers, S. P. Sander, M. W. Shephard, S. Sund, E. Ustinov, H. M. Worden, and J. Worden, "TES Level 2 Algorithm Theoretical Basis Document (ATBD)," NASA Goddard Space Flight Center, Greenbelt, MD, 2004. [Online]. Available: http://eospso.gsfc.nasa.gov/eos_homepage/for_scientists/atbd/.

[8] S. A. Clough and F. X. Kneizys, "Convolution algorithm for the Lorentz function," *Appl. Opt.*, vol. 18, pp. 2329–2333, 1979.

[9] F. X. Kneizys, S. A. Clough, and E. P. Shettle, "Atmospheric attenuation of laser radiation," *Proc. SPIE*, vol. 420, 1983.

[10] S. A. Clough, M. J. Iacono, and J.-L. Moncet, "Line-by-line calculation of atmospheric fluxes and cooling rates: Application to water vapor," *J. Geophys. Res.*, vol. 97, pp. 15 761–15 785, 1992.

[11] W. M. Elsasser, *Heat Transfer by Infrared Radiation in the Atmosphere, Harvard Meteorol. Studies*. Cambridge, MA: Harvard Univ. Press, 1942, vol. 6.

[12] X. Wu and W. L. Smith, "Emissivity of rough sea surface for 8–13 mm: Modeling and verification," *Appl. Opt.*, vol. 36, pp. 2609–2619, 1997.

[13] W. L. Smith, R. O. Knuteson, H. E. Revercomb, W. Feltz, H. B. Howell, W. P. Menzel, N. Nalli, O. Brown, J. Brown, P. Minnett, and W. McKeown, "Observations of the infrared radiative properties of the ocean—Implications for the measurement of sea surface temperature via satellite remote sensing," *Bull. Amer. Meteorol. Soc.*, Jan. 1996.

[14] K. Masuda, T. Takashima, and Y. Takayama, "Emissivity of pure and sea waters for the model sea surface in the infrared window regions," *Remote Sens. Environ.*, vol. 24, pp. 313–329, 1988.

[15] R. L. Kurucz, "The solar spectrum: Atlases and line identifications," in *Laboratory and Astronomical High Resolution Spectra*. ser. ASP Conference Series, A. Sauval, R. Blomme, and N. Grevesse, Eds. San Francisco, CA: Astron. Soc. Pacific Coast, 1995, vol. 81, pp. 17–31.

[16] ——, "Synthetic infrared spectra," in *Infrared Solar Physics*, vol. 154, D. M. Rabin and J. T. Jefferies, Eds., Norwell, MA, 1992.

[17] M. R. Gunson, M. M. Abbas, M. C. Abrams, M. Allan, L. R. Brown, T. L. Brown, A. Y. Chang, A. Goldman, F. W. Irion, L. L. Lowes, E. Mahieu, G. L. Manney, H. A. Michelsen, M. J. Newchurch, C. P. Rinsland, R. J. Salawitch, G. P. Stiller, G. C. Toon, Y. L. Yung, and R. Zander, "The Atmospheric Trace Molecule Spectroscopy (ATMOS) experiment: Deployment on the Atlas Space Shuttle missions," *Geophys. Res. Lett.*, vol. 23, pp. 2333–2336, 1996.

[18] C. P. Rinsland, G. K. Yie, M. R. Gunson, R. Zander, and M. C. Abrams, "Mid-infrared extinction by sulfate aerosols from the Mt. Pinatubo eruption," *J. Quant. Spectrosc. Radiat. Transf.*, vol. 52, pp. 241–252, 1994.

[19] J.-L. Moncet and S. A. Clough, "Accelerated monochromatic radiative transfer for scattering atmospheres: Application of a new model to spectral radiance observations," *J. Geophys. Res.*, vol. 102, pp. 21 853–21 866, 1997.

[20] S. S. Kulawik, J. Worden, A. Eldering, K. Bowman, H. Gunson, G. Osterman, L. Zhang, D. Jacob, S. A. Clough, M. W. Shephard, and R. Beer, "Implementation of cloud retrievals for Tropospheric Emission Spectrometer (TES) atmospheric retrievals. Part I. Description and characterization of errors on trace gas retrievals,", 2005. In preparation.

[21] W. O. Gallery and S. A. Clough, "FFTSCAN: A program for spectral smoothing using Fourier transforms," Phillips Lab., Hanscom AFB, MA, PL-TR-92-2131, 1992.

[22] R. N. Beer, "New apodizing functions for Fourier spectrometry," *J. Opt. Soc. Amer.*, vol. 66, pp. 259–264, 1976.

[23] K. W. Bowman, H. M. Worden, and R. Beer, "Instrument line-shape modeling and correction for off axis detectors in Fourier-transform spectrometry," *Appl. Opt.*, vol. 39, pp. 3765–3773, 2000.

[24] R. Beer, K. W. Bowman, B. M. Fisher, M. R. Gunson, R. G. Holm, M. Luo, D. M. Rider, E. Sarkissian, S. S. Kulawik, D. A. Tremblay, and H. M. Worden, "Instrument Calibration Report, Volumes 1 and 2," JPL, Pasadena, CA, D-26533, 2003.

[25] H. M. Worden and K. W. Bowman, "TES Level 1B Algorithm Theoretical Basis Document," NASA Goddard Space Flight Center, Greenbelt, MD, 1999. [Online]. Available: http://eospso.gsfc.nasa.gov/eos_homepage/for_scientists/atbd.

[26] H. M. Worden, R. Beer, K. Bowman, B. Fisher, M. Luo, E. Sarkissian, D. Tremblay, and J. Zong, "TES level 1 algorithms: Interferogram processing, geolocation, radiometric,and spectral calibration," *IEEE Trans. Geosci. Remote Sens.*, vol. 44, no. 5, pp. 1288–1296, May 2006.

[27] N. A. Scott and A. Chedin, "A fast line-by-line method for atmospheric absorption computations: The automatized atmospheric absorption atlas," *J. Appl. Meteorol.*, vol. 20, pp. 802–812, 1981.

[28] B. H. Armstrong, "Spectrum line profiles: The Voigt function," *J. Quant. Spectrosc. Radiat. Transf.*, vol. 7, pp. 61–88, 1967.

[29] G. P. Anderson, S. A. Clough, F. X. Kneizys, J. H. Chetwynd, and E. P. Shettle, "AFGL atmospheric constituent profiles (0–120 km)," Air Force Geophys. Lab., Hanscom AFB, MA, AFGL-TR-86-0110, 1986.

[30] L. S. Rothman, A. Barbe, D. C. Benner, L. R. Brown, C. Camy-Peyret, M. R. Carleer, K. V. Chance, C. Clerbaux, V. Dana, V. M. Devi, A. Fayt, J.-M. Flaud, R. R. Gamache, A. Goldman, D. Jacquemart, K. W. Jucks, W. J. Lafferty, J.-Y. Mandin, S. T. Massie, V. Nemtchinov, D. A. Newnham, A. Perrin, C. P. Rinsland, J. Schroeder, K. M. Smith, M. A. H. Smith, K. Tang, R. A. Toth, J. V. Auwera, P. Varanasi, and K. Yoshino, "The HITRAN molecular spectroscopic database: Edition of 2000 including updates through 2001," *J. Quant. Spectrosc. Radiat. Transf.*, vol. 82, pp. 5–44, 2003.

[31] L. S. Rothman, D. Jacquemart, A. Barbe, D. C. Benner, M. Birk, L. R. Brown, M. R. Carleer, C. Chackerian, Jr, K. Chance, V. Dana, V. M. Devi, J.-M. Flaud, R. R. Gamache, A. G. Goldman, J.-M. Hartmann, K. W. Jucks, A. G. Maki, J. Y. Mandin, S. Massie, J. Orphal, A. Perrin, C. P. Rinsland, M. A. H. Smith, R. A. Toth, J. V. Auwera, P. Varanasi, and G. Wagner, "The HITRAN 2004 molecular spectroscopic database," *J. Quant. Spectrosc. Radiat. Transf.*, 2006, to be published.

[32] R. A. Toth, "Water vapor measurements between 590 and 2582 cm^{-1}: Line positions and strengths," *J. Mol. Spectrosc.*, vol. 190, pp. 379–396, 1998.

[33] L. S. Rothman, R. R. Gamache, R. H. Tipping, C. P. Rinsland, M. A. H. Smith, D. C. H. Benner, V. M. Devi, V. J.-M. Flaud, C. Camy-Peyret, A. Perrin, A. Goldman, S. T. Massie, L. R. Brown, and R. A. Toth, "The HITRAN molecular database: Editions of 1991 and 1992," *J. Quant. Spectrosc. Radiat. Transf.*, vol. 48, pp. 469–507, 1992.

[34] L. S. Rothman, R. L. Hawkins, R. B. Wattson, R. R. Wattson, and R. R. Gamache, "Energy-levels, intensities, and linewidths of atmospheric carbon-dioxide bands," *J. Quant. Spectrosc. Radiat. Transf.*, vol. 48, no. 5–6, pp. 537–566, 1992.

[35] F. Niro, T. von Clarmann, K. Jucks, and J. M. Hartmann, "Spectra bands calculations in central and wing regions of CO2IR between 10 and 20 μm. III: Atmospheric emission spectra," *J. Quant. Spectrosc. Radiat. Transf.*, vol. 90, pp. 61–76, 2005.

[36] M. L. Hoke, S. A. Clough, W. J. Lafferty, and B. W. Olson, "Line coupling in oxygen and carbon dioxide," in *Proc. IRS 88: Current Problems in Atmospheric Radiation*, J. Lenoble and J. F. Geleyn, Eds. Hampton, VA, 1989, pp. 368–371.

[37] L. L. Strow, D. C. Tobin, and S. E. Hannon, "A compilation of first-order line mixing coefficients for Co2 Q-branches," *J. Quant. Spectrosc. Radiat. Transf.*, vol. 52, pp. 281–294, 1994.

[38] G. Wagner, M. Birk, F. Schreier, and J.-M. Flaud, "Spectroscopic database for ozone in the fundamental spectral regions," *J. Geophys. Res.*, vol. 107, 2002.

[39] J.-M. Flaud, C. Piccolo, B. Carli, A. Perrin, L. H. Coudert, J.-L. Teffo, and L. R. Brown, "Molecular line parameters for the MIPAS (Michelson Interferometer for Passive Atmospheric Sounding) experiment" (in Russian and English), *Atmos. Oceanic Opt.*, vol. 16, pp. 172–182, 2003.

[40] J.-M. Flaud and S. A. Clough, private communication, 2005.

[41] B. Picquet-Varrault, J. Orphal, J.-F. Doussin, P. Carleer, and J.-M. Flaud, "Laboratory measurements of the ozone absorption coefficients in the midinfrared (10 mm) and ultraviolet (300–350 nm) spectral regions," *J. Phys. Chem.*, vol. 109, pp. 1008–1014, 2005.

[42] Q. J. Zou and P. Varanasi, "New laboratory data on the spectral line parameters in the 1–0 and 2–0 bands of (CO)-C-12-O-16 relevant to atmospheric remote sensing," *J. Quant. Spectrosc. Radiat. Transf.*, vol. 75, pp. 63–92, 2002.

[43] M. A. H. Smith, L. R. Brown, V. M. Devi, and T. J. Pittman, "CO broadening and shift parameters for tes," in *Proc. 8th HITRAN Database Conf.*, Cambridge, MA, Jun. 15–18, 2004.

[44] L. R. Brown, D. C. Benner, J. P. Champion, V. M. Devi, L. Fejard, R. R. Gamache, T. Gabard, J. C. Hilico, B. Lavorel, M. Loete, G. Mellau, A. Nikitin, A. S. Pine, A. Predoi-Cross, C. P. Rinsland, O. Robert, R. L. Sams, M. A. H. Smith, S. A. Tashkun, and V. G. Tyuterev, "Methane line parameters in HITRAN," *J. Quant. Spectrosc. Radiat. Transf.*, vol. 82, pp. 219–238, 2003.

[45] D. C. Benner, private communication, 2005.

[46] J.-M. Flaud, C. Piccolo, B. Carli, A. Perrin, L. H. Coudert, J. L. Teffo, and L. R. Brown, *Infrared Spectroscopy and the MIPAS (Michelson Interferometer for Passive Atmospheric Sounding) Experiment, Proc. 8th HITRAN Database Conf.*, Cambridge, MA, Jun. 16–18, 2004.

[47] A. Perrin, C. P. Rinsland, and A. Goldman, *J. Geophys. Res.*, vol. 104, pp. 18 661–18 666, 1999.

[48] S. T. Massie and A. Goldman, "Absorption parameters of very dense molecular spectra for the HITRAN compilation," *J. Quant. Spectrosc. Radiat. Transf.*, vol. 48, pp. 713–719, 1992.

[49] J. Ballard, W. B. Johnston, M. R. Gunson, and P. T. Wassel, "Absolute absorption coefficients of Clono2 infrared bands at stratospheric temperatures," *J. Geophys. Res.*, vol. 93, pp. 1659–1665, 1988.

[50] A. H. McDaniel, C. A. Cantrell, J. A. Davidson, R. E. Shetter, and J. G. Calvert, "The temperature dependent, infrared absorption cross-sections for the chlorofluorocarbons: CFC-11, CFC-12, CFC-13, CFC-14, CFC-22, CFC-113, CFC-114, and CFC-115," *J. Atmos. Chem.*, vol. 12, pp. 211–227, 1991.

[51] S. T. Massie, A. Goldman, A. H. McDaniel, C. A. Cantrell, J. A. Davidson, R. E. Shetter, and J. G. Calvert, "Temperature dependent infrared cross sections for CFC-11, CFC-12, CFC-13, CFC-14, CFC-22, CFC-113, CFC-114, and CFC-115," NCAR , Boulder, CO, Tech. Note N-358+STR, 1991.

[52] C. A. Cantrell, J. A. Davidson, A. H. McDaniel, R. E. Shetter, and J. G. Calvert, *Chem. Phys. Lett.*, vol. 148, pp. 358–363, 1988.

[53] P. Varanasi, A. Gopalan, and J. F. Brannon, Jr., "Infrared absorption coefficient data on SF6 applicable to atmospheric remote sensing," *J. Quant. Spectrosc. Radiat. Transf.*, vol. 48, pp. 141–145, 1992.

[54] P. Varanasi, "Absorption coefficients of CFC-11 and CFC-12 needed for atmospheric remote sensing and global warming studies," *J. Quant. Spectrosc. Radiat. Transf.*, vol. 48, pp. 205–219, 1992.

[55] ——, "Absorption spectra of HCFC-22 around 829 cm^{-1} at atmospheric conditions," *J. Quant. Spectrosc. Radiat. Transf.*, vol. 47, pp. 251–255, 1992.

[56] ——, private communication, 1997.

[57] P. Varanasi and V. Nemtchinov, "Thermal infrared absorption coefficients of CFC-12 at atmospheric conditions," *J. Quant. Spectrosc. Radiat. Transf.*, vol. 51, pp. 679–687, 1994.

[58] Z. Li and P. Varanasi, "Measurement of the absorption cross-sections of CFC-11 at conditions representing various model atmospheres," *J. Quant. Spectrosc. Radiat. Transf.*, vol. 52, pp. 137–144, 1994.

[59] P. Varanasi, Z. Li, V. Nemtchinov, and A. Cherukuri, "Spectral absorption-coefficient data on HCFC-22 and Sf6 for remote-sensing applications," *J. Quant. Spectrosc. Radiat. Transf.*, vol. 52, pp. 323–332, 1994.

[60] L. S. Rothman, C. P. Rinsland, A. Goldman, S. T. Massie, D. P. Edwards, J.-M. Flaud, A. Perrin, C. Camy-Peyret, V. Dana, J.-Y. Mandin, J. Schroeder, A. McCann, R. R. Gamache, R. B. Wattson, K. Yoshino, K. V. Chance, K. W. Jucks, L. R. Brown, V. Nemtchinov, and P. Varanasi, "The HITRAN molecular spectroscopic database and HAWKS (HITRAN atmospheric Workstation): 1996 edition," *J. Quant. Spectrosc. Radiat. Transf.*, vol. 60, pp. 665–710, 1998.

[61] J. J. Orlando, G. S. Tyndall, A. Huang, and J. G. Calvert, "Temperature dependence of the infrared absorption cross sections of the carbon tetrachloride," *Geophys. Res. Lett.*, vol. 19, pp. 1005–1008, 1992.

[62] J. Orphal, M. Morillon-Chapey, and G. Guelachvili, "High-Resolution absorption cross sections of chlorine nitrate in the N2 band region around 1292 cm^{-1} at stratospheric temperatures," *J. Geophys. Res.*, vol. 99, pp. 14 549–14 555, 1994.

[63] C. Clerbaux, R. Colin, P. C. Simon, and C. Granier, "Infrared cross sections and global warming potentials of 10 alternative hydrohalocarbons," *J. Geophys. Res.*, vol. 98, pp. 10 491–10 497, 1993.

[64] K. Smith, D. Newnham, M. Page, J. Ballard, and G. Duxbury, "Infrared band strengths and absorption cross-sections of HFC-32 vapor," *J. Quant. Spectrosc. Radiat. Transf.*, vol. 56, pp. 73–82, 1996.

[65] ——, "Infrared absorption cross-sections and integrated absorption intensities of HFC-134 and HFC-143a vapor," *J. Quant. Spectrosc. Radiat. Transf.*, vol. 59, pp. 437–451, 1998.

[66] N. Jacquinet-Husson, E. Ariè, J. Ballard, A. Barbe, L. R. Brown, B. Bonnet, C. Camy-Peyret, J. P. Champion, A. Chèdin, A. Chursin, C. Clerbaux, G. Duxbury, J.-M. Flaud, N. Fourrie, A. Fayt, G. Graner, R. Gamache, A. Goldman, V. Golovko, G. Guelachvilli, J. M. Hartmann, J. C. Hillico, G. Lefevre, O. V. Naumenko, V. Nemtchinov, D. A. Newnham, A. Nikitin, J. Orphal, A. Perrin, D. C. Reuter, L. Rosenmann, L. S. Rothman, N. A. Scott, J. Selby, L. N. Sinitsa, J. M. Sirota, A. M. Smith, K. M. Smith, V. G. Tyuterev, R. H. Tipping, S. Urban, P. Varanasi, and M. Weber, "The 1997 spectroscopic Geisa databank," *J. Quant. Spectrosc. Radiat. Transf.*, vol. 62, pp. 205–254, 1999.

[67] S. A. Clough, "The water vapor continuum and its role in remote sensing," in *Optical Remote Sensing of the Atmosphere, OSA Tech. Dig. Series*, vol. 2. Washington, DC, 1995, pp. 76–81.

[68] S. A. Clough, F. X. Kneizys, and R. W. Davies, "Line shape and the water vapor continuum," *Atmos. Res.*, vol. 23, pp. 229–241, 1989.

[69] F. Thibault, V. Menoux, R. L. Doucen, L. Rosenman, J.-M. Hartmann, and C. Boulet, "Infrared collision-induced absorption by O_2 near 6.4 microns for atmospheric applications: Measurements and empirical modeling," *Appl. Opt.*, vol. 35, pp. 5911–5917, 1996.

[70] W. J. Lafferty, A. M. Solodov, A. Weber, W. B. Olson, and J.-M. Hartmann, "Infrared collision-induced absorption by N2 near 4.3 microns for atmospheric applications: Measurements and empirical modeling," *Appl. Opt.*, vol. 35, pp. 5911–5917, 1996.

[71] M. W. Shephard, S. A. Clough, J. Delamere, E. J. Mlawer, D. C. Tobin, D. D. Turner, H. E. Revercomb, and R. Knuteson, "Line-by-line radiative transfer model (LBLRTM) validations,", 2006. In preparation.

[72] M. W. Shephard, A. Goldman, S. A. Clough, and E. J. Mlawer, "Spectroscopic improvements providing evidence of formic acid in AERI-LBLRTM validation spectra," *J. Quant. Spectrosc. Radiat. Transf.*, vol. 82, pp. 383–390, 2003.

[73] E. J. Mlawer, S. J. Taubman, P. D. Brown, M. J. Iacono, and S. A. Clough, "Radiative transfer for inhomogeneous atmospheres: RRTM, a validated correlated-K model for the longwave," *J. Geophys. Res.*, vol. 102, pp. 16 663–16 682, 1997.

[74] D. D. Turner, B. M. Lesht, S. A. Clough, J. C. Liljegren, H. E. Revercomb, and D. C. Tobin, "Dry bias and variability in Vaisala RS80-H radiosondes: The ARM experience," *J. Atmos. Oceanic Technol.*, vol. 20, pp. 117–132, 2003.

[75] D. D. Turner, D. C. Tobin, S. A. Clough, P. D. Brown, R. G. Ellingson, E. J. Mlawer, R. O. Knuteson, H. E. Revercomb, T. R. Shippert, W. L. Smith, and M. W. Shephard, "The QME AERI LBLRTM: A closure experiment for downwelling high spectral resolution infrared radiance," *J. Atmos. Sci.*, vol. 61, pp. 2657–2675, 2004.

[76] S. A. Tjemkes, T. Patterson, R. Rizzi, M. W. Shephard, S. A. Clough, M. Matricardi, J. Haigh, M. Hopfner, S. Payan, A. Trotsenko, N. Scott, P. Rayer, J. Taylor, C. Clerbaux, L. L. Strow, S. DeSouza-Machado, D. Tobin, and R. Knuteson, "The ISSWG line-by-line intercomparison experiment," *J. Quant. Spectrosc. Radiat. Transf.*, vol. 77, pp. 433–453, 2003.

[77] M. W. Shephard, S. A. Clough, J. Delamere, D. C. Tobin, D. D. Turner, H. E. Revercomb, R. Knuteson, and R. Beer, "Validation of Co_2 line parameters used in temperature retrievals," in *Fourier Transform Spectroscopy, OSA Tech. Dig*. Washington, DC, 2003, pp. 128–132.

[78] D. C. Tobin, L. L. Strow, W. J. Lafferty, and W. B. Olson, "Experimental investigation of the self- and N2-broadened continuum within the N2 band of water vapor," *Appl. Opt.*, vol. 35, pp. 4274–4734, 1996.

Author photos and biographies not available at the time of publication.